



The response of a simulated mesoscale convective system to increased aerosol pollution: Part I: Precipitation intensity, distribution, and efficiency



Michal Clavner*, William R. Cotton, Susan C. van den Heever, Stephen M. Saleeby, Jeffery R. Pierce

Department of Atmospheric Science, Colorado State University, Fort Collins, CO, USA

A B S T R A C T

Mesoscale Convective Systems (MCSs) are important contributors to rainfall in the High Plains of the United States and elsewhere in the world. It is therefore of interest to understand how different aerosols serving as cloud condensation nuclei (CCN) may impact the total amount, rates and spatial distribution of precipitation produced by MCSs. In this study, different aerosol concentrations and their effects on precipitation produced by an MCS are examined by simulating the 8 May 2009 “Super-Derecho” MCS using the Regional Atmospheric Modeling System (RAMS), a cloud-resolving model (CRM) with sophisticated aerosol and microphysical parameterizations. Three simulations were conducted that differed only in the initial concentration, spatial distribution, and chemical composition of aerosols. Aerosol fields were derived from the output of GEOS-Chem, a 3D chemical transport numerical model. Results from the RAMS simulations show that the total domain precipitation was not significantly affected by variations in aerosol concentrations, however, the pollution aerosols altered the precipitation characteristics. The more polluted simulations exhibited higher precipitation rates, higher bulk precipitation efficiency, a larger area with heavier precipitation, and a smaller area with lighter precipitation. These differences arose as a result of aerosols enhancing precipitation in the convective region of the MCS while suppressing precipitation from the MCS's stratiform-anvil. In the convective region, several processes likely contributed to an increase of precipitation. First, owing to the very humid environment of this storm, the enhanced amount of cloud water available to be collected overwhelmed the reduction in precipitation efficiency associated with the aerosol-induced production of smaller droplets which led to a net increase in the conversion of cloud droplets to precipitation. Second, higher aerosol concentrations led to invigoration of convective updrafts which enhanced precipitation in accordance to the convective invigoration hypothesis. The reduction in stratiform precipitation in the more polluted simulations was found to be attributed to the presence of greater aerosol number concentrations that reduced both collision-coalescence and riming. Analysis of back trajectory flow showed that the air feeding the stratiform-anvil originated within the free troposphere, by mesoscale ascent. Therefore, increased aerosol pollution at higher elevations impacted the stratiform precipitation formation within the simulated MCS. As a consequence, the more polluted simulations produced the smallest precipitation from the MCS stratiform-anvil region. In Part II the impact of aerosols on the severe winds produced by this storm is examined.

1. Introduction

An MCS is a complex of thunderstorms organized on a larger scale than the thunderstorms themselves with a shared stratiform-anvil (Cotton et al., 2010). MCSs can range in size from a multicellular thunderstorm having three or four cells, to a Mesoscale Convective Complex (MCC), the largest form of MCSs (Cotton et al., 2010). Maddox (1980) defined an MCC as a long-lived circular MCS with specific characteristics according to infrared satellite imagery. Maddox's (1980)

definition of an MCC is an MCS which (1) exhibits a cloud top temperature colder than $-52\text{ }^{\circ}\text{C}$ over an area exceeding $50,000\text{ km}^2$, (2) that is embedded within a larger area of $100,000\text{ km}^2$ with cloud top temperatures colder than $-32\text{ }^{\circ}\text{C}$, (3) these specifications need to be upheld for at least 6 h, and (4) the MCS must exhibit an eccentricity of at least 0.7 at the time of maximum extent. Seeking a more dynamically based definition of an MCC, Cotton et al. (1989) and later Olsson and Cotton (1997a, 1997b), concluded that a mature MCC “represents an MCS that is in a nearly balanced dynamical state and whose horizontal

* Corresponding author.

E-mail address: michalcl@atmos.colostate.edu (M. Clavner).

scale is comparable to or greater than a locally defined Rossby radius of deformation”.

Previous studies showed that MCS development, intensity and precipitation is dependent on environmental conditions such as the low level jet (LLJ) (Maddox, 1983), vertical wind shear (Rotunno et al., 1988), convective available potential energy (CAPE), and moisture (Tao et al., 1993). Only in recent years have numerical simulation studies examined the impacts of changing aerosol concentrations on MCS intensity and the precipitation produced by these systems. It has been found that increased concentrations of potential cloud condensation nuclei (CCN) can impact MCS intensity, propagation and precipitation via their impacts on the microphysical processes and, in turn, the dynamical feedbacks to the system (Khain et al., 2005; Tao et al., 2007; Li et al., 2009; Seigel et al., 2013; Lebo and Morrison, 2014). Numerical simulations have suggested an increase in mid-latitude MCS-produced precipitation in a more polluted environment due to the enhancement of cold precipitation processes such as ice vapor deposition and riming (Khain et al., 2005), convective invigoration of the updrafts (Andreae et al., 2004; Koren et al., 2005; Rosenfeld et al., 2008), and the production of larger rain drops which survived evaporation more readily below cloud base (Berg et al., 2008; Li et al., 2009; May et al., 2011). For a given amount of liquid water content, increased potential CCN concentrations nucleate more numerous and smaller cloud droplets (Twomey, 1974, 1977) leading to a suppression of warm rain formation by collision coalescence (Squires, 1958; Albrecht, 1989). In turn, more cloud water is lofted to higher levels and cold precipitation production is enhanced, thereby invigorating the convective updraft due to the latent heat release of freezing of supercooled drops, vapor deposition growth of ice particles, and riming (Andreae et al., 2004; van den Heever et al., 2006; Rosenfeld et al., 2008). Furthermore, enhanced riming within stronger updrafts produces larger hailstones which are found to shed more numerous and larger raindrops, contributing to the surface precipitation (Storer et al., 2010; Storer and van den Heever, 2013).

The effect of increased concentrations of potential CCN on MCS precipitation have been found to be dependent on environment conditions such as humidity (Khain et al., 2005; Tao et al., 2007) and vertical wind shear (Fan et al., 2009; Lebo and Morrison, 2014) due to the microphysical effects of increased aerosols and its dynamical feedback on the storm intensity. The impacts of higher aerosol concentrations on precipitation production from an MCS was found also to depend on the type of aerosol and its chemistry, size and distribution. For example, using only mineral dust as an aerosol, Seigel et al. (2013) identified a time dependent precipitation response to an increase in aerosol concentration. This was attributed to the bi-modal nature of the dust distribution, whereby, the smaller mode served as CCN while the coarser mode served as Giant CCN (GCCN) and Ice Nuclei (IN). During the first couple of hours of the MCS simulation, the presence of dust increased the precipitation due to presence of dust serving as GCCN, thus, enhancing warm rain production by collision-coalescence. However, early rainout led to a reduction of supercooled water aloft, which reduced the riming rates and the contribution of riming to the latent heat release. This, in turn, led to weaker updrafts, suppressed convective mass flux, and a reduction in total precipitation.

In this study, we seek additional insight into the impact of enhanced CCN concentrations on a mid-latitude MCS by simulating the variability of a spatially heterogeneous field of 12 aerosols species on a case-study MCS. Estimates of aerosol concentrations were derived from output of GEOS-Chem, a 3D chemical transport model (Bey et al., 2001). The case chosen for this study is the 8 May 2009 “Super Derecho” MCS and has been analyzed in several papers (Przybylinski et al., 2010; Coniglio et al., 2011; Coniglio et al., 2012; Keene and Schumacher, 2013; Weisman et al., 2013; Evans et al., 2014; Xu et al., 2015a, b). However, none of these studies examined the potential sensitivity of the storm characteristics to changes in aerosol concentrations. This study adds to the current body of work by examining the microphysical impacts of

increased concentrations of several different aerosols species on the precipitation production of the 8 May 2009 MCS. The case study is described in Section 2. The RAMS numerical model set up, the GEOS-Chem model and its output and implementation with in RAMS is described in Section 3. The results of changing aerosol concentration on the precipitation produced by the case study storm are presented in Section 4. In Part II the impact of aerosols on the severe winds produced by this storm is examined.

2. The 8 May 2009 MCS

The 8 May 2009 event has been characterized in previous studies (Coniglio et al., 2011; Weisman et al., 2013) as a leading-line, trailing stratiform (Houze et al., 1989; Parker and Johnson, 2000) bow-echo (Fujita, 1978). The MCS developed in western Kansas and moved south-southeastward to the southern Appalachians, traveling over a thousand miles in under 24 h (Coniglio et al., 2011; Storm Prediction Center (SPC)). Further details of the environment of the 8 May 2009 MCS and the evolution of the storm can be found in previous studies (Coniglio et al., 2011; Keene and Schumacher, 2013; Weisman et al., 2013).

In order to determine the MCS lifespan (genesis, mature, dissipation) and the convective structure of the MCS, satellite infrared cloud top temperature from the Geostationary Operational Environmental Satellite 12 (GOES-12) imagery and Weather Surveillance Radar, 1988, Doppler (WSR-88D) mosaic radar images of composite reflectivity were analyzed (Fig. 1). The first convective clouds prior to the MCS genesis stage occurred on May 8 shortly after 0300 UTC along the eastern slopes of the Rockies, which is a common location for MCS genesis in the High Plains of the United States (Cotton et al., 1983; Maddox, 1983; Velasco and Fritsch, 1987; Augustine and Caracena, 1994). The initial convective clouds then propagated eastward into Kansas, into a region with high precipitable water (PW), which was found to be anomalously high in comparison to other mid-latitude MCS environments (Coniglio et al., 2011). The region of high PW ($> 30 \text{ kg m}^{-2}$), which at first is confined to eastern Kansas, grew in extent and covered most of Kansas by 0600 UTC, most likely in association with the formation of the LLJ (Fig. 2) that supplied the region with moisture as well as appropriate wind shear. By 0700 UTC (Fig. 1a) the individual convective cells merged and deepened, signifying the genesis stage of the MCS (McAnelly and Cotton, 1986). The orientation of the initial MCS convection (Fig. 1d) was on the cold side of a surface boundary, also a common characteristic in an MCS environment (Maddox, 1983; Cotton et al., 1989).

During the next several hours the storm progressed eastwards while it grew in size both horizontally and in depth, and entered Missouri by 1000 UTC. The storm reached its maximum size at ~ 1200 UTC (Fig. 1b), signifying the storm's mature stage (Maddox, 1983). It was during this time when the MCS exhibited a pronounced bow echo (Fig. 1e). As the storm exited Missouri at ~ 1700 UTC, the cloud-top temperatures began to increase indicating that the convective cells within the MCS were beginning to dissipate (Fig. 1c). From the analysis of the IR imagery, the 8 May 2009 MCS embodies MCC-like characteristics by being more circular than linear; however, it does not exhibit a defined inner core of temperatures below -52C , and therefore does not comply with Maddox's criteria for a classic MCC.

The observed precipitation from the 8 May 2009 MCS was assessed according to the National Weather Service Advanced Hydrological Prediction Service (NWS-AHPS) River Forecast Centers (RFCs) gridded observation of accumulated 24 h precipitation. Data from 7 May 1200 UTC until 9 May 1200 UTC were plotted in order to capture the precipitation produced by the 8 May MCS (Fig. 3). This storm system produced large amounts of precipitation in both Kansas and Missouri, with areas receiving up to 115 mm of accumulated precipitation (Fig. 3). In this study, we examine how changes in the environmental aerosol concentrations can alter the precipitation produced by this system. A key feature of the 8 May 2009 system was the strong straight-

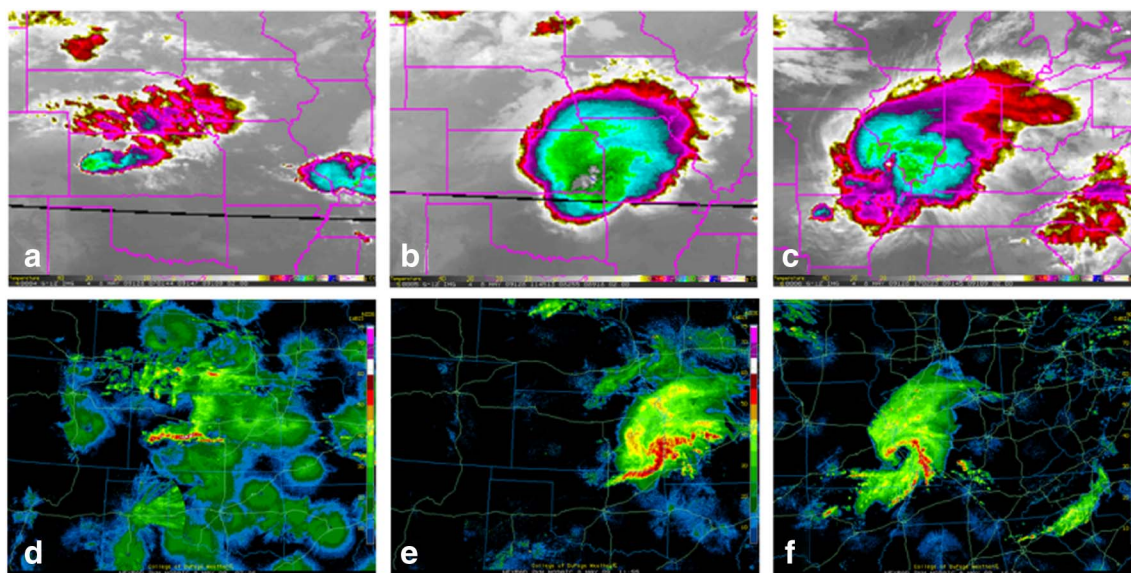


Fig. 1. Top: Satellite infrared cloud top temperature from the Geostationary Operational Environmental Satellite 12 (GOES-12) at (a) 0701 UTC, (b) 1145 UTC and (c) 1702 UTC. Bottom: Weather Surveillance Radar, 1988, Doppler (WSR-88D) mosaic radar images of composite reflectivity at (d) 0726 UTC, (e) 1155 UTC and (f) 1654 UTC.

line winds (derecho) (Johns and Hirt, 1987) produced by the storm. The sensitivity of the dynamics of the 8 May 2009 MCS, specifically the derecho strength, to changes in aerosols concentrations is examined in Part II.

3. Numerical model and experiment setup

3.1. Model configuration

The case study of the 8 May 2009 was simulated using the Colorado State University Regional Atmospheric Modeling System (RAMS) (Cotton et al., 2003; Saleeby and van den Heever, 2013). The RAMS model simulation was set up as a cloud resolving mesoscale model with three interactive model grids (Fig. 4). Grids 1 and 2's spatial areas were determined in order to simulate the synoptic and mesoscale environments, respectively. Grid 3's spatial area covers the entire domain of the simulated MCS from genesis to decay. All three grids were set up with 55 vertical levels and a model top height extending to 19 km above ground level (AGL) with a vertical grid spacing of 50 m at the lowest vertical grid level stretched to a maximum of 500 m. The simulation duration was 24 h from 0000 UTC May 8, 2009 until 0000 UTC May 9, 2009 and was initialized using the North American Regional Reanalysis

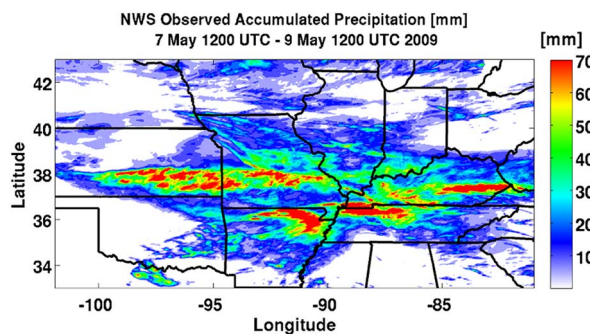


Fig. 3. National Weather Service Advanced Hydrological Prediction Service (NWS-AHPS) River Forecast Centers (RFCs) gridded observation of accumulated 24 h precipitation [mm] from 8 May at 1200 UTC to 9 May at 1200 UTC 2009.

(NARR) data from 8 May 2009 at 0000 UTC. RAMS soil moisture in all 3 grids was also initialized with NARR surface soil moisture. Further information on the RAMS simulation set up is presented in Table 1.

RAMS uses a sophisticated two-moment, bin-emulating, bulk microphysics scheme that prognoses both mass and number concentration for eight hydrometeor classes: cloud, drizzle, rain, pristine ice, snow,

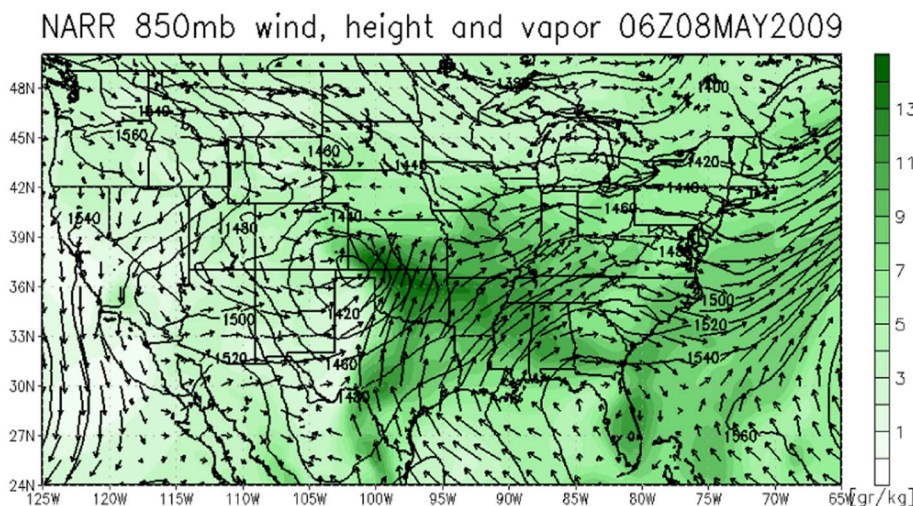


Fig. 2. NARR 850 mb plot of horizontal wind (vectors) geopotential heights [m] (black contours) and specific humidity [g kg^{-1}] (shaded) for 8 May 2009 at 0000 UTC.

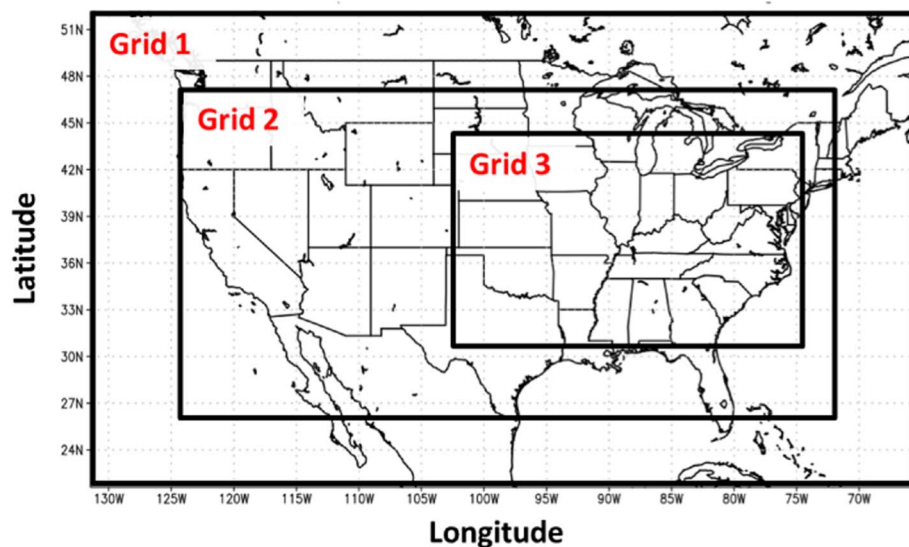


Fig. 4. Regional Atmospheric Modeling System (RAMS) nested grid set up locations for the parent grid (Grid 1) and the nested grids: Grid 2 and 3.

Table 1
RAMS configuration and options.

Model Aspects	Settings
Grid	Arakawa C grid (Mesinger and Arakawa, 1976) Three grids Horizontal grid: Grid 1: $\Delta x = \Delta y = 40$ km 120 \times 80 points Grid 2: $\Delta x = \Delta y = 8$ km 507 \times 267 points Grid 3: $\Delta x = \Delta y = 1.6$ km 1422 \times 822 points Vertical grid: 55 levels, 12 below 1 km AGL $\Delta z =$ variable Minimum $\Delta z = 50$ m, maximum $\Delta z = 500$ m Vertical stretch ratio = 1.09 Model top ≈ 19 km
Time step	Grid 1: 20 s Grid 2: 10 s Grid 3: 3.33 s
Simulation durations	24 h: 8th May 0000 UTC–9th May 0000 UTC
Initialization	North American Regional Reanalysis (NARR)
Boundary conditions	Radiative lateral boundary (Klemp and Wilhelmson, 1978)
Microphysics scheme	Lateral and top model nudging from NARR Two-moment bulk microphysics (Meyers et al., 1997) Eight hydrometeor classes (Saleeby and Cotton, 2004) DeMott et al. (2010) ice nucleation parameterization Microphysical budget tracking (Saleeby and van den Heever, 2013)
Turbulence scheme	Smagorinsky (1963) deformation K closure scheme with stability modifications by Lilly (1962) and Hill (1974)
Radiation scheme	Two-stream radiation parameterization (Harrington, 1997; Harrington et al., 1999)
Surface scheme	Land Ecosystem- Atmospheric Feedback (LEAF-3) (Walko et al., 2000) with soil moisture from the NARR data
Aerosol treatment	12 aerosol species from the Goddard Earth Observing System – Chemistry (GEOS-Chem, Bey et al., 2001)

aggregates, graupel, and hail (Meyers et al., 1997; Saleeby and Cotton, 2004, 2008; Saleeby and van den Heever, 2013). The RAMS microphysical scheme was set up with the option of budget tracking of microphysical processes, which is critical in analyzing the precipitation microphysics and processes within the simulation (Saleeby and van den Heever, 2013). Aerosol data from the 3D chemistry transport model, Goddard Earth Observing System Chemistry (GEOS-Chem) v9.01.03 (Bey et al., 2001) were incorporated into RAMS. The GEOS-Chem model and GEOS-Chem simulations are described in Section 3.2. The implementation of GEOS-Chem aerosols as potential CCN and IN into

RAMS is described in Section 3.3.

3.2. GEOS-Chem model and simulations

GEOS-Chem is a global/regional three-dimensional chemical transport model driven by the assimilated meteorological observations from the Goddard Earth Observing System (GEOS) of the NASA Global Modeling Assimilation Office (GMAO), the GEOS-5 product (Bey et al., 2001). GEOS-Chem simulates the emission, chemical interactions, transport and removal of 64 gas and particle-phase species. Emissions fields and model spatial characteristics are described in detail in Stevens and Pierce (2014). Twelve aerosol species were used in this study: three inorganic aerosols (sulfate, nitrate and ammonia) and eight organic aerosols (primary hydrophilic organic carbon, primary hydrophilic black carbon, primary hydrophobic organic carbon and primary hydrophobic black carbon as well as 5 secondary organic aerosol (SOA) groups. For this study, two GEOS-Chem simulations were performed: the first with anthropogenic emissions included and the second with anthropogenic emissions turned off, thereby creating two separate aerosol concentration data sets for North America. The first data set included therefore only aerosols from natural emissions, while the second data included emissions from both natural and anthropogenic sources.

3.3. Implementation of GEOS-Chem aerosols into RAMS

GEOS-Chem model output of 8 May 2009 0000Z, corresponding to the RAMS simulation initialization time, was used in order to represent “realistic” horizontally heterogeneous aerosol concentrations with varying hygroscopicity. The concentrations of the different aerosol species depends on location and altitude. Therefore, the incorporation of several aerosols species into RAMS generated a more comprehensive three dimensional representation of an aerosol concentration population. All 12 of the aerosol species were assumed to have a lognormal distribution with a geometric mean radius of 60 nm and a geometric standard deviation of 1.8. The twelve aerosol species were introduced into RAMS as three different internally mixed aerosol groups based on their CCN activity, represented by Kappa. Kappa is defined as a non-dimensional single hygroscopicity parameter ranging from 0 (non-hygroscopic) to 1.4 (very hygroscopic) (Petters and Kreidenweis, 2007). The three groups were categorized as: inorganics (highly-CCN-active), hygroscopic organics and non-hygroscopic organics with kappa values of 0.6, 0.12 and 0, respectively. The grouping of the twelve aerosol species into three groups was motivated by reducing the RAMS

computation time while still representing different aerosols types that differ in their nucleation potential. Each of the aerosol groups was set to be radiatively inactive and hence, the direct effect (Haywood and Boucher, 2000; Koren et al., 2004) of these aerosols was not represented in the model simulations. This configuration was chosen in order to isolate the effects of changes in aerosol quantities on cloud microphysics and on the simulated MCS dynamics and precipitation.

The three aerosol groups potentially can serve as either CCN or IN as follows. In order to represent cloud nucleation competition among the three aerosol groups the three groups are assumed to be internally mixed and a concentration-weighted kappa is calculated at the time of aerosol activation. The fraction of activated aerosols from the total aerosol concentration at a given grid point is then calculated using a lookup table, which was created offline using Lagrangian parcel model runs with internally mixed aerosols (Ward et al., 2010; Ward and Cotton, 2011; Letcher and Cotton, 2014). Aerosol concentrations serving as IN were calculated as a function of the total number of non-sea salt aerosols with diameters $> 0.5 \mu\text{m}$ (DeMott et al., 2010) of each of the three aerosol groups, separately. The heterogeneous ice nucleation scheme used in the RAMS simulations captures IN via deposition nucleation, condensation freezing, and immersion freezing (DeMott et al., 2010; Saleeby and van den Heever, 2013). Therefore, aerosol particles outputted from GEOS-Chem can potentially serve as CCN and IN, depending on the aerosol characteristics.

3.4. Experimental design: RAMS simulations

In order to examine the impact of the presence of anthropogenic aerosols concentrations and increased aerosol concentrations on the RAMS simulated case study MCS, three sensitivity simulations were performed (Table 2). The only difference among the three simulations at the time of RAMS model initialization was the GEOS-Chem aerosol concentration and spatial distribution. The first simulation, labeled as “CLEAN”, was initialized with aerosol concentrations from the GEOS-Chem simulation containing aerosols from only natural emissions (no anthropogenic sources). The second simulation, labeled as “POLLUTED”, was initialized with aerosol concentrations from the GEOS-Chem containing aerosols from both anthropogenic and natural emissions. In order to examine a more highly polluted scenario, the third simulation, labeled as “ $5 \times$ POLLUTED”, was initialized with the same aerosol distribution as the POLLUTED simulation, but with aerosol number and mass multiplied by a factor of five. The $5 \times$ POLLUTED simulation was motivated by past studies that looked at the impact of increased aerosol concentration $> 6000 \text{ cm}^{-3}$ (Storer et al., 2010; Carrio and Cotton, 2011).

The vertical profiles of the average total aerosol number concentrations and the concentration weighted kappa value at the time of the MCS genesis (0630 UTC) in the three simulations are presented in Fig. 5. In order to examine the heterogeneous distribution of both concentration and chemical composition of the aerosols within the three simulations, Fig. 5 also shows the vertical profiles of the upper and lower 10th percentile of the total aerosol concentration (Fig. 5a) and the estimated kappa values (Fig. 5b). Differences in the aerosol distribution between the GEOS-Chem data containing both anthropogenic emission and natural emission in comparison to just natural emissions are most evident in the lower levels due to the regional

sources of anthropogenic aerosols within the boundary layer. The difference between the CLEAN and POLLUTED aerosol concentration decreases as a function of height. It is important to note that at 0630 UTC, for the $5 \times$ POLLUTED simulation, the aerosol concentrations were larger by a factor of 5 at all vertical levels. The GEOS-Chem aerosols were incorporated in all three of the RAMS grids (Fig. 4) at the time of model initialization, after which, the only sources of aerosols are the advection of aerosols from the coarser to finer grids as well as the formation of aerosols due to the evaporation of cloud droplets.

4. Simulation results

4.1. Isolating the simulated MCS

In all three simulations, convective elements not associated with the MCS did occur in the analyzed grid (Grid 3). In order to perform statistical analysis, such as computing the precipitation produced solely from the MCS, data from the other convective elements were numerically filtered out. The filtering technique used in this study was motivated by past studies that separated a region into cloudy and clear sky using cloud top temperature from infrared satellite imagery. Similar to Igel et al. (2014), cloud objects were identified using a binary function, labeling a continuous area of the domain as cloudy or clear according to prescribed cloud property thresholds. In this study, only cloudy pixels that could be considered a part of the MCS were of interest. Therefore, a dominant criterion for labeling a grid column as cloudy was set according to cloud top temperature, a salient feature in MCSs (Maddox, 1980; Jirak et al., 2003). The filtering technique also incorporated the two dimensional parameters of precipitation rate [mm h^{-1}] and vertically-integrated total condensate (VITC) [kg m^{-2}]. In this study, data analyzed from the simulated MCS were taken from MCS genesis at 0630 UTC until 1730 UTC, after which the method for isolating the MCS was less reliable due to the dissipation of the system and subsequent fragmentation of the MCS' stratiform-anvil as well as close proximity of the storm to neighboring convection.

4.2. Comparisons with observations

VITC was analyzed in order to identify the geographic location, evolution, spatial extent and temporal timing of the simulated MCS. Qualitatively, the three simulations produced similar MCS genesis times, storm sizes, propagation locations and life spans. For brevity, only plots of VITC for the POLLUTED simulation are presented for 0700 UTC, 1200 UTC and 1700 UTC (Fig. 6a, b, c). In all three of the simulations, MCS development occurred in western Kansas at 0630 UTC and quickly organized under a shared stratiform-anvil at 0700 UTC (Fig. 6a). The convective cores exhibited a west-east orientation, similar to the observed composite radar reflectivity (Fig. 1d). As the convective cores propagated east-southeastward with time, the stratiform-anvil spread out and grew to a horizontal scale comparable to an MCC (~ 1200 UTC) (Fig. 6b), similar to the observed infrared satellite imagery (Fig. 1b). At 1200 UTC, the higher VITC values, indicative of the presence of convective cores, were located in the southeastern corner of Kansas, similar to the composite radar reflectivity (Fig. 1e). Synthetic satellite imagery has also been found to be a useful tool for validating simulated cloud fields with observations from GOES imagery (Grasso

Table 2
RAMS Simulations.

Simulation	Simulation Name	Characteristics
1	CLEAN	Initialized with a heterogeneous aerosol distribution using output from the GEOS-Chem simulation with only natural emissions.
2	POLLUTED	Initialized with a heterogeneous aerosol distribution using output from the GEOS-Chem simulation with both anthropogenic and natural emissions.
3	$5 \times$ POLLUTED	Initialized with GEOS-Chem aerosols with 5 times as much aerosols as in the Polluted simulation.

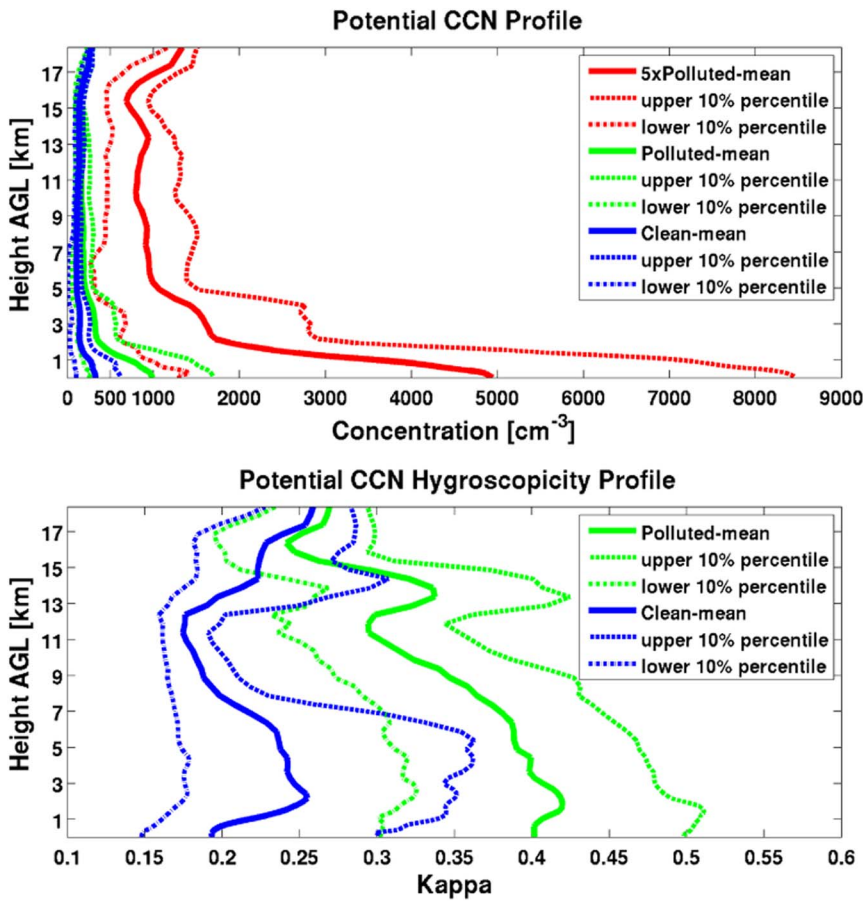


Fig. 5. Top: Vertical profile of the mean (solid line) aerosol concentration for the three simulations at the time of the MCS genesis (0630 UTC): Clean (blue), Polluted (green) and 5 × Polluted (red). Bottom: Vertical profile of the number concentration weighted mean (solid line) kappa values for the two simulations: Clean (blue) and Polluted (green). The 5 × Polluted featured the same kappa value estimates as that of the POLLUTED simulation due to the multiplication of all aerosols species by a factor of five. For both panels, the vertical profile of the upper and lower 10th percentiles are represented in the dash-dotted and dashed line, respectively. (For interpretation of the references to color in this figure legend, the reader is referred to the web version of this article.)

and Lindsey, 2011; Jankov et al., 2011; Grasso et al., 2013). Synthetic imagery was produced by coupling RAMS output data with a radiative transfer numerical model in order to simulate a cloud top temperature for a given wavelength. In this study the wavelength of 10.7 μm was chosen in order to compare the synthetic satellite imagery to GOES-12 infrared cloud top temperature. Fig. 6d, e and f presents the synthetic

GOES-12 imagery at 1200 UTC from the three simulations. A comparison between the synthetic satellite imagery and the observed GEOS-12 image at 1145 UTC (Fig. 1b) shows that RAMS was successful in simulating the 8 May 2009 MCS's location, size, and values of infrared cloud top temperatures. The onset of MCS dissipation occurred shortly after 1430 UTC in all three simulations as the MCS stratiform-anvil

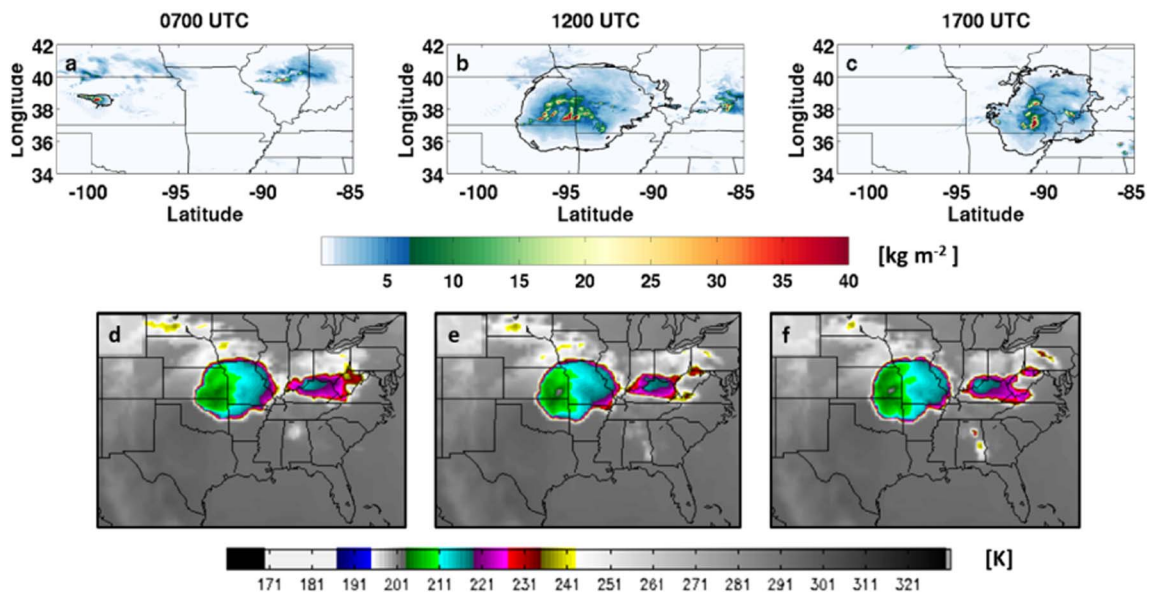


Fig. 6. (a) RAMS vertically integrated total condensate [kg m^{-2}] (shaded) for the Polluted simulation at 0700 UTC, (b) 1200 UTC and (c) 1700 UTC. Contoured in black is the region which is considered to be part of the MCS following the isolation guidelines described in Section 4.1. Synthetic GOES-12 cloud top temperature imagery [K] at 1200 UTC for the (d) Clean (e) Polluted and (f) 5 × Polluted.

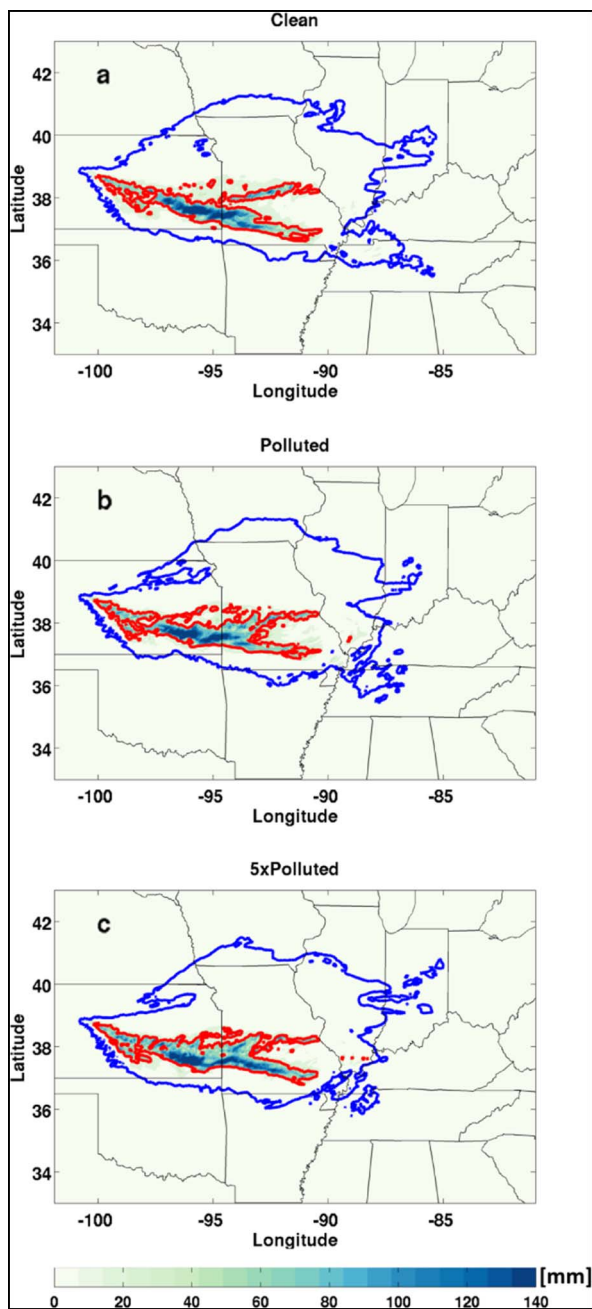


Fig. 7. Total accumulated precipitation (shaded) [mm], 0.05 mm isopleth (contoured in blue) and the 50 mm isopleth (contoured in red) from the three MCS simulations: (a) Clean, (b) Polluted and (c) $5 \times$ Polluted. (For interpretation of the references to color in this figure legend, the reader is referred to the web version of this article.)

became fragmented and the MCS horizontal scale began to decrease in size (Fig. 6c).

The simulated total accumulated precipitation from the entire analysis period for the three simulations is illustrated in Fig. 7. All three simulations produced similar spatial distributions of the surface precipitation to that observed (Fig. 4). The highest accumulated precipitation occurred over central Kansas, south-central Kansas and central Missouri, coinciding with the observations. The difference in the spatial distribution of accumulated precipitation among the simulations due to aerosol impacts is discussed in Section 4.3.

4.3. Response of simulated MCS precipitation to changes in aerosol concentrations

4.3.1. Total precipitation

By the end of the analysis period (0630–1730 UTC), all three of the simulations produced similar amounts of volumetric precipitation ($\sim 8 \cdot 10^9 \text{ m}^3$), with differences of $< 1\%$ among the simulations. Although the total volumetric precipitation did not differ substantially, the spatial distribution of accumulated precipitation among the three simulations did change as a function of aerosol number concentration. An increase in aerosol concentration produced heavier precipitation over a larger area and lighter precipitation over a smaller area. This is evident in the number of grid points containing precipitation totals above thresholds between 0 and 140 mm (99% of the data) in 5 mm precipitation intervals (Fig. 8). The $5 \times$ POLLUTED exhibited a smaller number of grid points with lighter accumulated precipitation (0–25 mm) and more numerous grid points with heavier accumulated precipitation amounts (30–135 mm), relative to the CLEAN simulation. These findings indicate that increased aerosol number concentrations led to a shift from lighter to heavier precipitation rates. A similar trend is seen between the CLEAN and the POLLUTED simulation, however, the differences were smaller in magnitude. This shift is further indicated in Fig. 7, where the area of total MCS precipitation (contoured in blue in Fig. 8) was 8% and 9.5% less in the POLLUTED and $5 \times$ POLLUTED simulations than in the CLEAN simulation, respectively. However, the spatial extent of the area with accumulated total precipitation > 50 mm (90th percentile, contoured in red in Fig. 7) was greater in the POLLUTED and $5 \times$ POLLUTED simulations by 9.6% and 21.8%, respectively. Therefore, the simulated storm's precipitation production varied as a function of aerosol loading.

Precipitation efficiency is an indication of how efficient a storm as a whole is in converting water vapor into precipitation. The precipitation efficiency of the simulated MCS was calculated using two methods: (Albrecht, 1989) calculating the ratio between the differences in hydrometeor mass gain and loss to hydrometeor mass gain (Khain et al., 2005), and (Altartatz et al., 2014) determining the ratio between the surface rainfall rate to the rate of condensation and deposition (the Cloud Microphysics Precipitation Efficiency (CMPE) (Sui and Li, 2005)). Both calculations showed a shift to higher precipitation efficiencies in the more polluted simulations throughout the analysis period (not shown). The differences in precipitation rates, area of precipitation and precipitation efficiency are now explained by analyzing the contributions of the convective and stratiform precipitation to the total precipitation.

4.3.2. Convective and Stratiform precipitation

MCS precipitation can be characterized into two regions: convective and stratiform-anvil, which differ in dynamical properties, microphysical processes and precipitation rates (Leary and Houze, 1979). The division into the two regions utilized for the simulated MCS data was based on two parameters: surface precipitation rate [mm h^{-1}] and the column maximum vertical velocity [m s^{-1}], that was adapted from the criteria set by Churchill and Houze (1984), Tao et al. (1993) and Alexander and Cotton (1998). The MCS partitioning into convective and stratiform-anvil regions was done as follows. A grid column is defined as convective if ANY of the following are true: (1) the precipitation rate is two times the average background precipitation rate with an added criterion that the precipitation rate must be $> 10 \text{ mm h}^{-1}$ in order to eliminate stratiform precipitation that exhibits the same trend; (2) precipitation rates are $> 25 \text{ mm h}^{-1}$; (3) all grid columns adjacent to a flagged convective column (according to either (1) or (2)) are also flagged convective; or (4) the maximal vertical velocity exceeds 5 m s^{-1} .

The background average precipitation rate was calculated from an area around the grid column of interest using 6 grid points in each direction, which corresponds to an area of $\sim 370 \text{ km}^2$ and is similar to

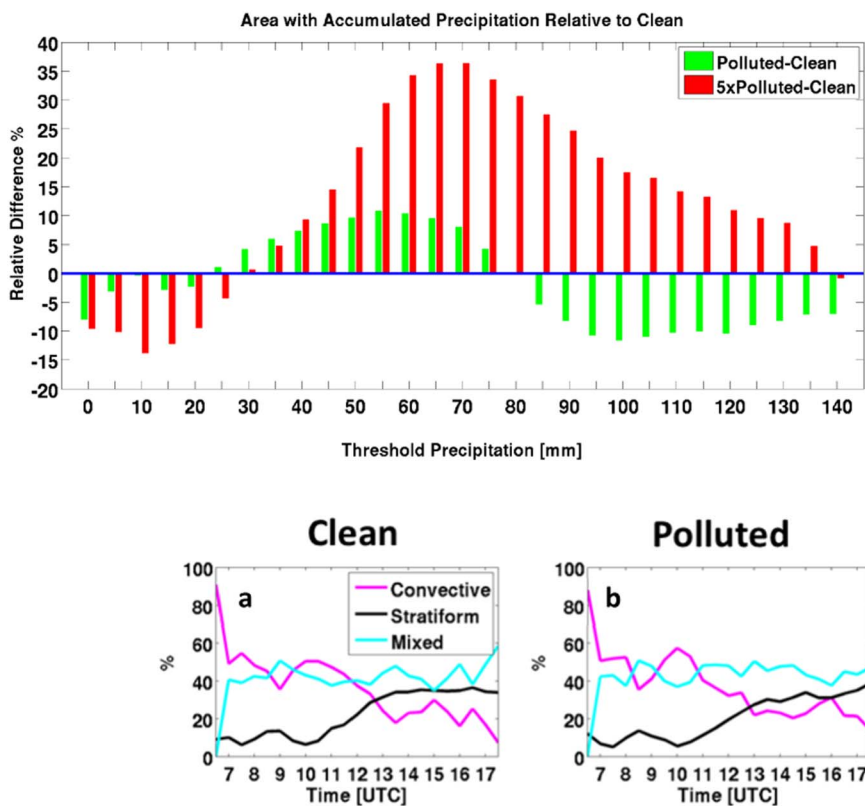


Fig. 8. Relative difference in the areas containing accumulated precipitation above a given value [mm] in the Polluted (green) and the 5 × Polluted (red) simulations in comparison to the Clean simulation. (For interpretation of the references to color in this figure legend, the reader is referred to the web version of this article.)

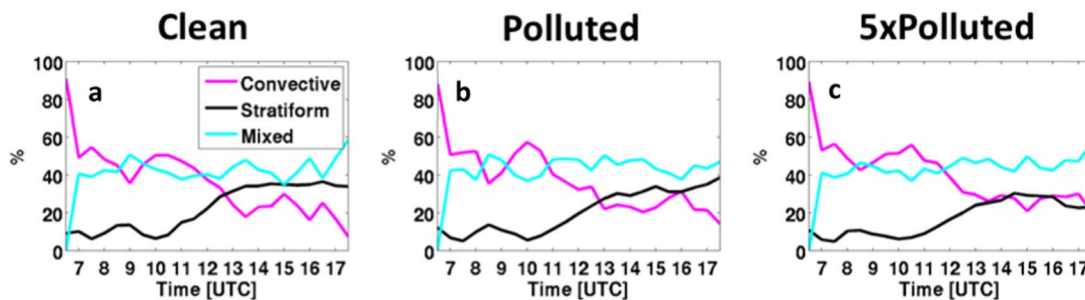


Fig. 9. Relative contribution of the volumetric precipitation rate [$\text{m}^3 \text{s}^{-1}$] from the each of the regions: convective (magenta), mixed (cyan) and stratiform-anvil (black) to the total volumetric MCS precipitation in the (a) Clean, (b) Polluted and (c) 5 × Polluted simulations. (For interpretation of the references to color in this figure legend, the reader is referred to the web version of this article.)

the background area size defined in Churchill and Houze (1984). A third region referred to as “mixed” for cumulative variables such as accumulative precipitation was defined as a grid column which was defined as convective (stratiform-anvil) at analysis file output time t , but as stratiform-anvil (convective) in the previous output file time, $t-1$. Therefore, for a given grid point, the accumulated precipitation over 30 min will be defined as convective (stratiform) only if that grid point was defined as such in two consecutive output times, otherwise, the grid point is labeled as “mixed”. The relative contributions to the total volumetric precipitation rate [$\text{m}^3 \text{s}^{-1}$] from the three regions (Fig. 9) show that the convective region is the dominant contributor to the total volumetric precipitation rate during the first half of the analysis period (0630–1230 UTC). However, after 1230 UTC, the highest contributor to the precipitation shifts from convective to stratiform-anvil in the CLEAN and POLLUTED simulations. This shift from convective to stratiform-anvil precipitation as the system matures is in agreement with previous findings of MCC precipitation characteristics (McAnelly and Cotton, 1986). A shift to a larger contribution from the stratiform-anvil region to the total volumetric precipitation also occurs in the 5 × POLLUTED simulation, however at 2 h later than in both the CLEAN and POLLUTED simulations, indicating that the 5 × POLLUTED simulation had the highest precipitation yield from convective precipitation and smallest from the stratiform precipitation throughout the analysis period.

The comparison of the accumulated volumetric precipitation among the regions shows that enhanced aerosol concentrations led to an increase in convective precipitation, a decrease in stratiform precipitation and negligible change in the mixed region throughout the analysis period (Fig. 10). By the end of the analysis period, the POLLUTED and 5 × POLLUTED simulations produced 2.43% and 15% more convective precipitation, 3.5% and 5% more mixed precipitation and 10% and 25% less stratiform precipitation in comparison to the CLEAN

simulation, respectively. Therefore, even though changes in the aerosol concentrations among the three simulations had little effect on the total amount of accumulated volumetric precipitation, it did change the precipitation contributions from the convective and stratiform-anvil regions (Fig. 10). The differences among the simulations in the mixed region were found to be negligible (Fig. 9) in comparison to the convective and stratiform regions, and therefore, are not discussed further.

The trends in volumetric precipitation are a function of both the precipitation area and precipitation rates (Kane et al., 1987). In order to examine the aerosol impacts on the two components of volumetric precipitation, the mean precipitation rates [mm h^{-1}], and the total precipitation area of each region: convective and stratiform [km^2] are compared (Fig. 11). Furthermore, Fig. 11 also shows the area of the non-precipitating points, in order to compare between the total MCS area and the MCS precipitating area within each of the regions in the three simulations. The higher convective volumetric precipitation in 5 × POLLUTED is predominantly attributed to the precipitation rates (on average 23.7% higher relative to CLEAN, Fig. 11a) and not the areal extent of the convective region (on average 3.3% higher relative to CLEAN, Fig. 11c). The higher volumetric precipitation in the stratiform-anvil of the CLEAN simulation is attributed to both higher precipitation rates from the time of MCS’s mature stage until the end of the analysis period (on average 11% higher relative to 5 × POLLUTED, Fig. 11b) as well as a larger precipitating area within the stratiform-anvil region (on average 20% larger relative to 5 × POLLUTED, Fig. 11d). Therefore, increased aerosol concentrations limited the precipitation formation processes within the stratiform-anvil with the 5 × POLLUTED simulation as seen by the smaller area with stratiform precipitation (solid lines, Fig. 11d) versus the larger area extent of the stratiform-anvil region (dashed lines, Fig. 11d). In order to understand why greater aerosol concentrations in the POLLUTED and 5 × POLLUTED simulations caused an increase in the convective precipitation and decreased

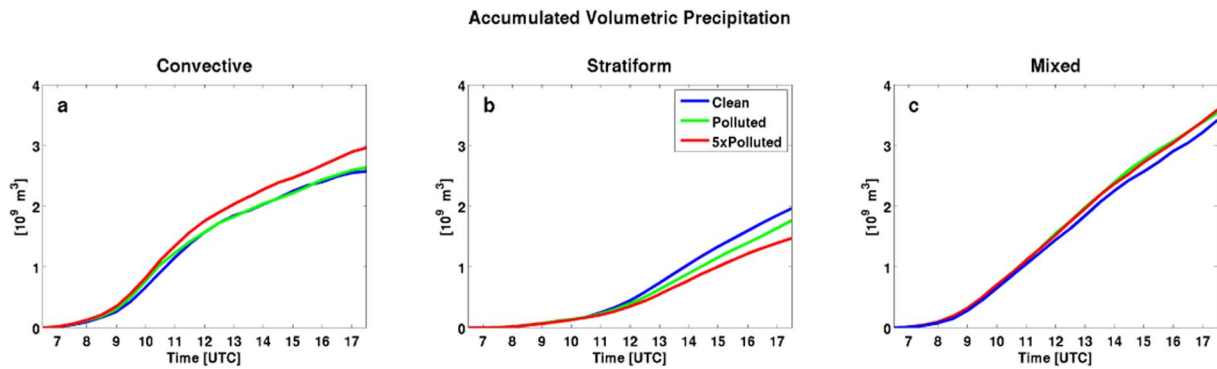


Fig. 10. Accumulated volumetric precipitation from the (a) convective, (b) stratiform and (c) mixed regions for the three simulations: Clean (blue), Polluted (green) and $5 \times$ Polluted (red) as a function of time. (For interpretation of the references to color in this figure legend, the reader is referred to the web version of this article.)

the stratiform precipitation formation mechanisms, the precipitation formation mechanisms for the two regions composing the MCS are now examined.

4.3.3. Precipitation processes: warm versus cold microphysics

The column integrated mean collision coalescence and riming rates [kg s^{-1}] were calculated in the convective and stratiform-anvil regions for each simulation as a function of time. The relative differences in these rates within the POLLUTED and $5 \times$ POLLUTED simulations in comparison the CLEAN (Fig. 12) indicate that the enhanced precipitation from the convective region and the reduction from the stratiform-anvil region are attributed to changes in both the warm rain processes of collision-coalescence as well as cold precipitation formation via riming and are discussed in the following sections.

4.3.3.1. Stratiform-anvil region. Increased aerosol concentrations led to a decrease in total volumetric stratiform precipitation (Fig. 10), primarily due to a smaller fraction of the stratiform-anvil which produced precipitation (Fig. 11d), indicative of changes within the precipitation formation efficiency. During the majority of the analysis period, the $5 \times$ POLLUTED simulation exhibited reduced collision-coalescence and riming rates [kg s^{-1}] in the stratiform-anvil region in comparison to the CLEAN simulation (Fig. 12d). On the other hand, the POLLUTED simulation alternated from having higher and lower rates of precipitation formation throughout the analysis period, in comparison to the CLEAN simulation (Fig. 12c). The decrease in both precipitation formation mechanisms in the simulations with greater aerosol number concentrations can be explained by the formation of more numerous (Fig. 13b) yet smaller cloud droplets (Fig. 13a), which reduced the efficiency of collision-coalescence and the formation of

warm rain. The reduction in collision coalescence yielded more cloud mass (Fig. 13c) to be lofted to higher levels and freeze, producing a larger number (Fig. 13e) of smaller pristine ice hydrometers (Fig. 13d). The smaller pristine ice aggregated to produced more numerous (Fig. 13k) yet smaller aggregates (Fig. 13j), the main ice hydrometer to undergo riming within the stratiform-anvil region (not shown). Therefore, the smaller cloud droplets reduced both collision coalescence and riming rates within the stratiform-anvil region.

Previous numerical studies have shown that an increase in aerosol number concentrations impacted the precipitation formation within the stratiform-anvil of an MCS by altering the hydrometeor distribution within the convective outflow of the storm composing the anvil (e.g. Tao et al., 2012). However, other studies have shown that the outflow of hydrometeors from the deep convective cells is the sole air source of the anvil only during the development stages of the storm and as the storm matures, slow ascending mesoscale ascent develops, which forms the stratiform-anvil of the MCS (Cotton et al., 1995, 2010; Houze, 2004). This slow ascent was found to be present in the middle and upper troposphere in a broad region surrounding the convective cores, and it is formed in response to the deep convergence layer associated with the diabatic heating profile of an MCS (e.g. Cotton et al., 1989). Therefore, higher aerosol number concentrations at higher elevations AGL may potentially impact the formation of stratiform precipitation.

In order to determine the source of the hydrometeors (slow ascent or convective outflow) within the stratiform-anvil region in this case study, a Lagrangian model (LM) (Grasso, 1996) was used to compute the backwards parcel trajectories from different regions within the stratiform-anvil. The starting points for these parcels within the stratiform-anvil were subjectively placed around the convective cores at time 1230 UTC (Fig. 14). This time was chosen since 1230 UTC was the time

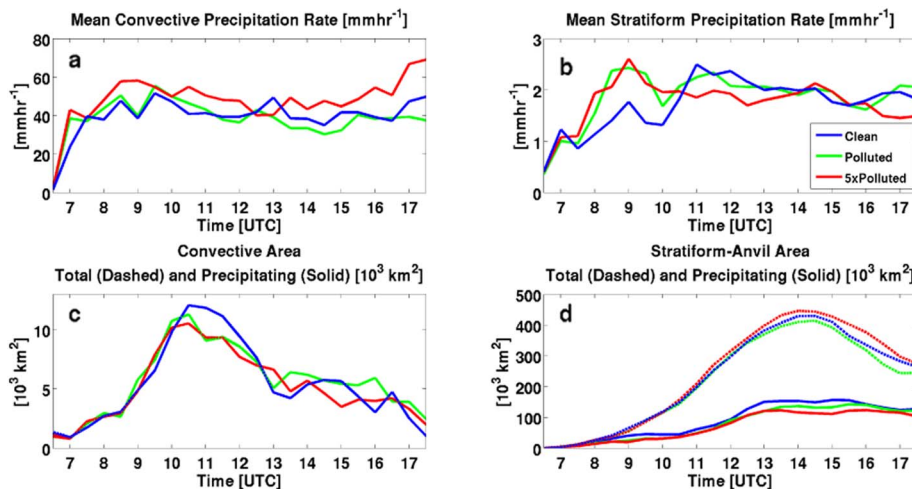


Fig. 11. For the three simulations Clean (blue), Polluted (green) and $5 \times$ Polluted (red) simulations: (a) Mean convective precipitation rate [mm h^{-1}] as a function of time. (b) Mean stratiform precipitation rate [mm h^{-1}] as a function of time. (c) Total area of the convective region [km^2] (dashed) and area with convective precipitation [km^2] (solid). (d) Total area of the stratiform-anvil region [km^2] (dashed) and area with stratiform precipitation [km^2] (solid). Note, nearly 100% of the convective region was precipitating, therefore, in panel c, the dashed and solid lines overlap. (For interpretation of the references to color in this figure legend, the reader is referred to the web version of this article.)

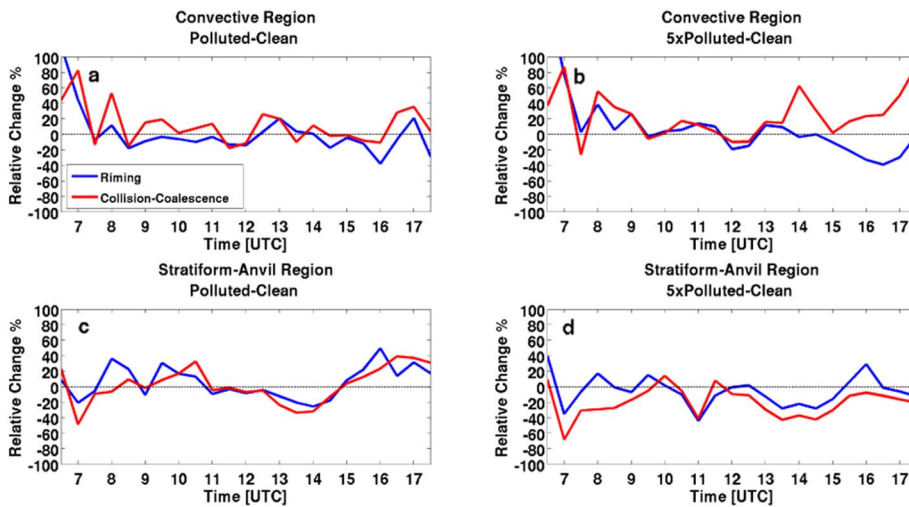


Fig. 12. Relative differences in the mean column integrated riming and collision coalescence (C-C) rates [kg s^{-1}] in the polluted simulations relative to Clean: for the Polluted simulation in the (a) convective region and (c) stratiform-anvil region and for the $5 \times$ Polluted simulation in the (b) convective region and (d) stratiform-anvil region.

where the MCS stratiform-anvil became an important contributor to the MCS precipitation (Fig. 9). Each region (Fig. 14) represented a grid volume with an area of $10 \times 10 \text{ km}^2$ with approximately 35 vertical profiles (corresponding to ~ 35 horizontal grid points with a horizontal spacing of 1.6 km). From the 7 locations, parcels within cloudy grid boxes (total condensate $\geq 0.01 \text{ g kg}^{-1}$) were inserted into the LM. RAMS was rerun for the period of 90 min from 1100 to 1230 UTC and the 3D wind components (u , v and w) from the Eulerian RAMS Grid 3 were saved at each time step. Values of the extracted variables were then transferred, by a tri-linear spatial interpolation scheme within the LM, to the parcel's location. Advection of a parcel was accomplished with the use of the 4th order Runge-Kutta method and a time step of 3.33 s, corresponding to the output time of RAMS velocity data; consequently, interpolation in time was not needed. The time interval of 90 min was chosen in order to be able to examine the presence of the slow ascending mesoscale ascent which travels over a hundred kilometers horizontally at these slow ascent speeds.

Results of the back trajectory analysis for the regions 2, 4 and 6 are presented by 2D trajectory of parcel height as a function of time and the maximum vertical velocity along the 90 min trajectory of each parcel for the three regions (Fig. 15). These three regions were chosen here since they represent three different cloud structures as seen from the seven sampled regions. Upstream of the convective region, the stratiform-anvil clouds were composed primarily of upper-level stratiform clouds (example: Region 2, Fig. 16a). North of the convective region, thicker stratiform clouds with cloud bases as low as 3 km AGL were evident (example: region 4 Fig. 16b). Downstream of the convective region, thin stratiform clouds with cloud bases of 3 km AGL and cloud top heights below 6 km AGL, below a shallow stratiform-anvil were evident (example: region 6 Fig. 16c). The composition of hydrometeors in the various regions is as follows. Within the elevated stratiform cloud the hydrometeors are only ice-phase hydrometeors (Fig. 16a and c). Within the low-level stratus cloud only liquid-phase hydrometeors are present (Fig. 16c). Mixed-phase hydrometeors prevail within the deep stratiform cloud (Fig. 16b). At this time, the CLEAN and $5 \times$ POLLUTED simulations exhibited similar trends in cloud structure to that in the POLLUTED simulation. For brevity, only the vertical profiles of the hydrometeor mixing ratio and results from the LM of the POLLUTED simulation for regions 2, 4 and 6 are shown.

The results from the LM model indicate that the main air source feeding the MCS's stratiform-anvil for the three regions shown here, is slow mesoscale ascent, as seen by both the parcel elevation with time and maximum vertical velocities below 2 m s^{-1} (Fig. 15). The source of parcels from convective outflow is present only at higher altitudes in regions 4 and 6, as seen by the higher vertical velocities (Fig. 15e, f) as well as the parcel's elevation with time (Fig. 17b, c). Precipitation is

present in both the low level stratiform cloud (region 6: Fig. 16c) and the deep mixed phase cloud (region 4: Fig. 16b). Therefore, both mesoscale ascent and convective outflow impact the precipitation formation mechanisms within the stratiform-anvil region of the simulated MCS. The 90 min back trajectory analysis shows that the mesoscale ascent originates 1–9 km AGL, depending on the parcels origin height. For this reason, varying aerosol concentrations at these higher altitudes impact the hydrometeor distribution, and the precipitation formation within this flow. The $5 \times$ POLLUTED simulation contained higher aerosol concentrations both within the boundary layer and within the free troposphere (Fig. 5), which explains the formation of the smaller and more numerous cloud droplets which hampered precipitation processes within the stratiform-anvil region. Above the boundary layer ($\sim 1 \text{ km AGL}$), the aerosol concentrations in the CLEAN and POLLUTED simulations were similar (Fig. 5), since the additional anthropogenic aerosols in the GEOS-Chem model output incorporated in the POLLUTED simulation introduced higher aerosol concentrations predominantly near the surface. Therefore, the regions of mesoscale ascent originating above the boundary layer feeding the deep stratiform-anvil contained similar aerosol concentrations in the CLEAN and POLLUTED simulations (Fig. 5). This explains why the $5 \times$ POLLUTED simulations consistently had lower precipitating formation rates leading to a 25% less stratiform precipitation by the end of the analysis period in comparison to the CLEAN simulation, while the POLLUTED simulation only exhibited a deficiency of 10%.

4.3.3.2. Convective region. The spatial and temporal mean vertical profiles of collision-coalescence and riming (Fig. 17) shows that both these rates were increased within the convective region of the $5 \times$ POLLUTED simulation throughout the entire vertical column relative to both the CLEAN and POLLUTED simulations. These increases within the $5 \times$ POLLUTED simulation are larger at the elevations which these processes are more prevalent, indicating that the increases in aerosol concentrations impacted the efficiency but not the depth these processes occurred. In comparison, the POLLUTED simulation only exhibited higher collision-coalescence rates relative to CLEAN. Increased aerosol concentration led to enhanced collision coalescence and riming in the $5 \times$ POLLUTED simulation and enhanced collision coalescence in the POLLUTED simulation (Fig. 17) due to the increase in cloud droplet concentration (Fig. 18h), despite the decrease in cloud mixing ratio (Fig. 18i). This is explained by the fact that the enhanced concentration of cloud water available to be collected by rain drops and hail within the $5 \times$ POLLUTED simulation overwhelmed the reduction in the collection efficiency associated with the aerosol-induced production of smaller cloud droplets (Fig. 18g), leading to a net increase in the conversion of

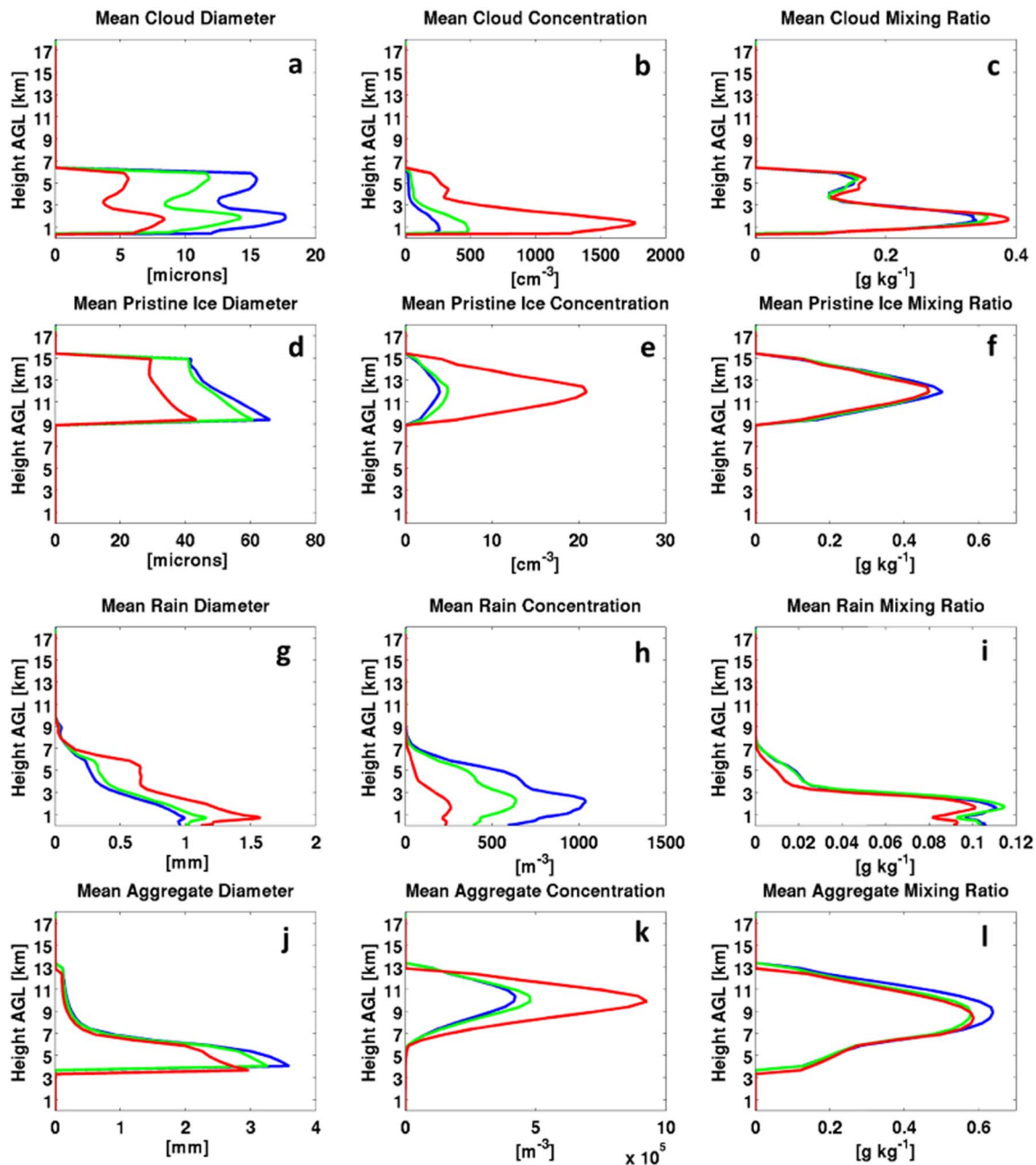


Fig. 13. Spatial and temporal means during 0630–1730 UTC in the stratiform-anvil region of: (a) cloud droplet diameter [microns], (b) cloud droplet concentration [cm^{-3}], (c) cloud mixing ratio [g kg^{-1}], (d) pristine ice diameter [microns], (e) pristine ice concentration [cm^{-3}], (f) pristine ice mixing ratio [g kg^{-1}], (g) rain diameter [mm], (h) rain concentration [m^{-3}], (i) rain mixing ratio [g kg^{-1}], (j) aggregates diameter [mm], (k) aggregates concentration [m^{-3}] and (l) aggregates mixing ratio [g kg^{-1}] for the Clean (blue), Polluted (green) and $5 \times$ Polluted (red) simulations.

cloud droplets to precipitation. The same process occurred in the POLLUTED simulation, however only for collision-coalescence. The smaller aerosol concentrations in the POLLUTED simulation in comparison to the $5 \times$ POLLUTED along with the enhanced collision-coalescence in comparison to CLEAN led to a depletion of cloud number concentration at higher levels (Fig. 18h). As a result, the riming rates are smaller in the POLLUTED simulation even when compared with the CLEAN simulation (Fig. 17). The result of increased aerosol number concentration therefore led to fewer (Fig. 18b) yet larger rain drops (Fig. 18a) in both polluted simulations and less (Fig. 18e) yet larger hail (Fig. 18d) in the $5 \times$ POLLUTED simulation. The formation of larger rain drops reduced the potential for evaporation below cloud base (Fig. 18c) owing to their net reduction in surface area (van den Heever and Cotton, 2004), thereby further enhancing the amount of surface

accumulated convective precipitation.

Another impact of changing aerosol concentrations on convective precipitation formation has been found to be through convective invigoration. Past studies have shown that increased aerosol number concentration may lead to stronger updraft velocities by altering the amount of latent heat release as evidenced in the review article by Tao et al. (2012), which in turn could increase precipitation formation by transporting liquid water to higher levels (e.g. Andreae et al., 2004; Koren et al., 2005; van den Heever and Cotton, 2007; Storer and van den Heever, 2013) and increasing hydrometeor residence time within an updraft by sustaining larger hydrometers (Bowen, 1951). In this study, the strongest maximum vertical velocities, which are representative of the convective region, were found within the $5 \times$ POLLUTED (Fig. 19a) simulation which is consistent with the

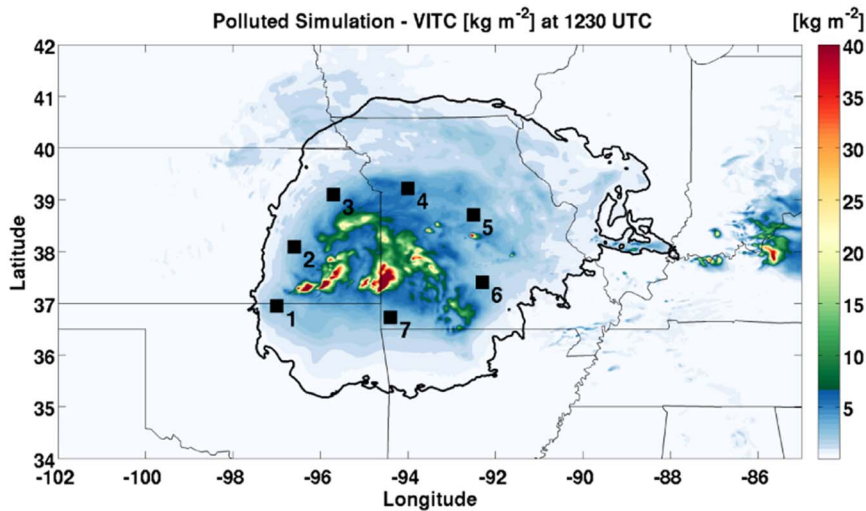


Fig. 14. Vertically-Integrated Total Condensate (VITC) at 1230 UTC with the locations of the $10 \times 10 \text{ km}^2$ grid volumes within the stratiform-anvil (locations 1–7). This image is for the Polluted simulation.

convective invigoration hypothesis. Fig. 19 presents the spatial and temporal mean of the maximum updraft speeds as well as a relative probability density function of updraft speeds at 5 km AGL, showing that greater aerosol concentrations produced stronger updraft speeds. Therefore both microphysical impacts of increased aerosol concentrations on precipitation formation and their dynamical feedback on convective invigoration contributed to enhanced convective precipitation within this simulated case study.

5. Discussion

In this study, changes in aerosol concentrations both within and above the boundary layer impacted the precipitation characteristics of the simulated MCS by altering the amount of precipitation produced by the convective and stratiform-anvil regions of the storm. The higher aerosol concentrations were found to increase the size of the area with

heavier accumulated precipitation and decrease the area with lighter accumulated precipitation. This shift in precipitation rates was attributed to higher aerosol concentrations increasing the amount of convective precipitation and decreasing the amount of stratiform precipitation produced by the MCS. Enhanced convective precipitation arising from an increased aerosol number concentration has been found in past numerical simulations of deep convection due to enhanced warm rain production (Seigel et al., 2013), formation of larger raindrops with reduced low level evaporation rates (Berg et al., 2008; Li et al., 2009; Storer et al., 2010; Storer and van den Heever, 2013) as well as more efficient cold rain production (Khain et al., 2005; van den Heever and Cotton, 2007; Tao et al., 2012). An increase in aerosol number concentrations can increase precipitation production by the dynamical feedback of convective invigoration. There are two facets to this hypothesis: (Albrecht, 1989) convective invigoration due to suppression of warm rain production and (Altartatz et al., 2014) increased

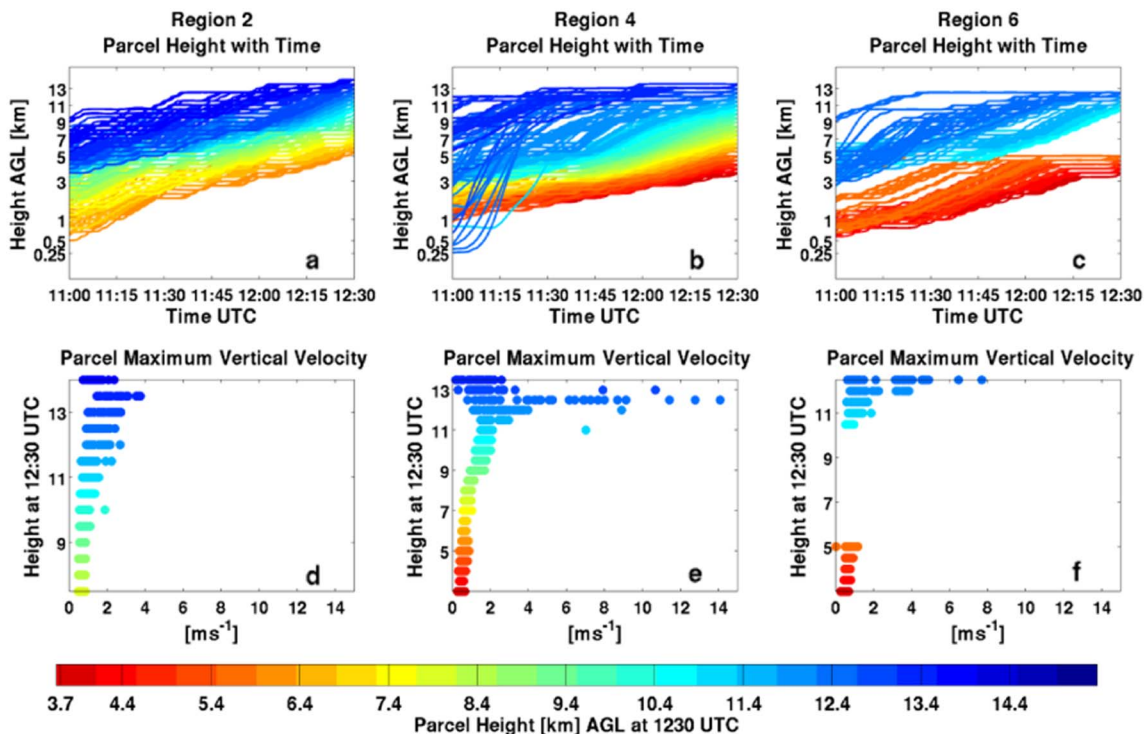


Fig. 15. Top row: 90 min (1100–1230 UTC) parcel height trajectory for regions (a) 2, (b) 4 (b) and (c) 6. Bottom row: scatter plot of the parcel's maximum updraft velocity during the 90 min trajectory for regions (d) 2, (e) 4 (e) and (f) 6. All data point color coded according to the parcel's back trajectory originated height at 1230 UTC.

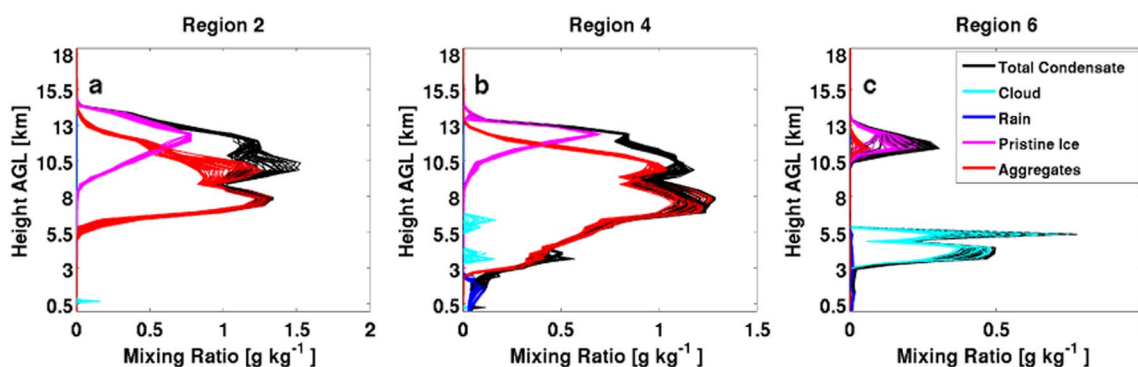


Fig. 16. Vertical profiles (~ 35) within three of the regions: (a) region 2, (b) region 4 and (c) region 6 of total hydrometeor mixing ratio (black) as well as the individual mixing ratios of the dominant hydrometeors: cloud (cyan), rain (blue), pristine ice (magenta) and aggregates (red). (For interpretation of the references to color in this figure legend, the reader is referred to the web version of this article.)

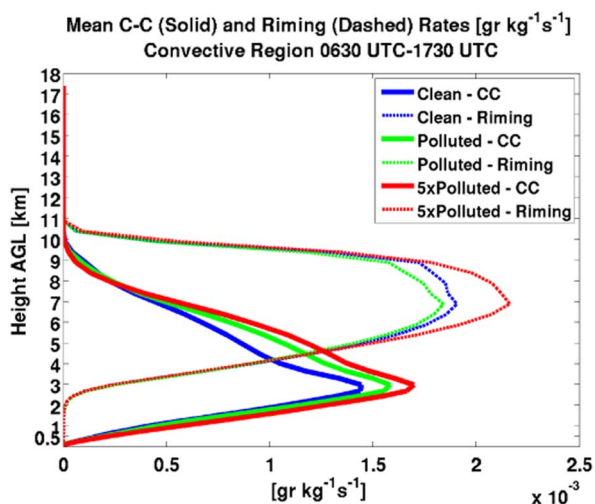


Fig. 17. Spatial and temporal mean within the convective region of collision coalescence (CC) (solid lines) and riming (dashed lines) during 0630–1730 UTC for the Clean (blue), Polluted (green) and $5 \times$ Polluted (red) simulations. (For interpretation of the references to color in this figure legend, the reader is referred to the web version of this article.)

latent heat release of condensation. High concentrations of aerosols lead to high concentrations of cloud droplets, they suppress warm rain formation, transport greater quantities of cloud droplets to supercooled levels, which freezes and ice particle riming is enhanced, thereby releasing greater amounts of latent heat, and the added buoyancy invigorates the updrafts of cumuli, and the invigorated updrafts process more water thereby enhancing rainfall (Andreae et al., 2004; Khain et al., 2005; van den Heever et al., 2006; van den Heever and Cotton, 2007; Rosenfeld et al., 2008; Carrio and Cotton, 2011; Fan et al., 2013; Storer and van den Heever, 2013; Altaratz et al., 2014). The second facet of the convective invigoration hypothesis is what is now called “condensation invigoration”. There is modeling and theoretical evidence that high concentrations of pollution-sized hygroscopic aerosol can invigorate the updrafts of purely warm clouds (Kogan and Martin, 1994; Altaratz et al., 2014; Seiki and Nakajima, 2014; Saleeby et al., 2015; Sheffield et al., 2015). The theory is that high concentrations of cloud droplets formed on numerous pollution-sized aerosol exhibit greater net surface areas upon which condensation occurs, thereby enhancing net vapor deposition rates which leads to enhanced latent heat release by condensation in cumuli. Recent studies (e.g. Grabowski, 2016) suggest that at heights above 3 km above cloud base where droplet collection can be prevalent, supersaturations can exceed nominal near-cloud-base values, which can lead to appreciable enhancement of condensation in a polluted cloud relative to a clean cloud. Thus latent heat by condensation of droplets can be enhanced enough to

invigorate updrafts, lead to greater amounts of condensed water, produce broader, longer-lived convective updrafts and thereby enhance rainfall. At this time the relative contribution of “condensational invigoration” versus convective invigoration by mixed-phase processes in MCSs has not been determined. In this study, since the MCS formed in a highly humid environment, collision coalescence was enhanced with a moderate increase in pollution aerosols and both collision coalescence and riming in the highly polluted simulation, it is likely that the condensational invigoration played a key role in the convective invigoration found in this study.

Past studies have shown that changes in aerosol number concentrations altered the stratiform precipitation formation within an MCS primarily due to the impacts on convective outflow. It has been shown that a decrease in convective precipitation can increase the outflow to the stratiform-anvil, thereby increasing the stratiform precipitation production (e.g. Tao et al., 2007). In this study, the opposite was found, where the increased aerosol pollution led to a reduction in stratiform precipitation and an increase in convective precipitation. The reduction in stratiform precipitation was found to be due to the impact of aerosols on hydrometeors not only within the convective outflow but also within slow mesoscale ascent. The roles of these flows were determined by performing back-trajectory analysis from locations within the stratiform-anvil. The results of this analysis indicates that changes in aerosol concentrations at higher levels impacts the formation of precipitation within the stratiform-anvil due to the changes in cloud nucleation within mesoscale ascent that originates at heights above the boundary layer (1–5 km AGL). This study emphasizes that aerosol impacts on stratiform precipitation are not only due to changes within the hydrometeor distribution within the convective outflow, but also in the formation of cloud droplets within slow slantwise ascending regions.

6. Conclusions

In this study, the microphysical effect of increased aerosol concentrations on the precipitation produced by a simulated case study MCS, the 8 May 2009 “Super-derecho” MCS, was examined. A set of three RAMS simulations was conducted: CLEAN, POLLUTED and $5 \times$ POLLUTED, in which the initial aerosol distribution, concentration and chemical composition differed based on the output of a 3D chemical model, GEOS-Chem. Twelve specific aerosol particle types from GEOS-Chem were inserted into RAMS in order to represent a more “realistic” horizontally heterogeneous aerosol concentration field with varying nucleation potential, thereby introducing nucleation competition among the different aerosol species. The CLEAN simulation contained only aerosol concentrations from non-anthropogenic sources, the POLLUTED included aerosols from both anthropogenic and non-anthropogenic sources and the $5 \times$ POLLUTED had the same distribution as in the POLLUTED simulation, but increased by a factor of five. All

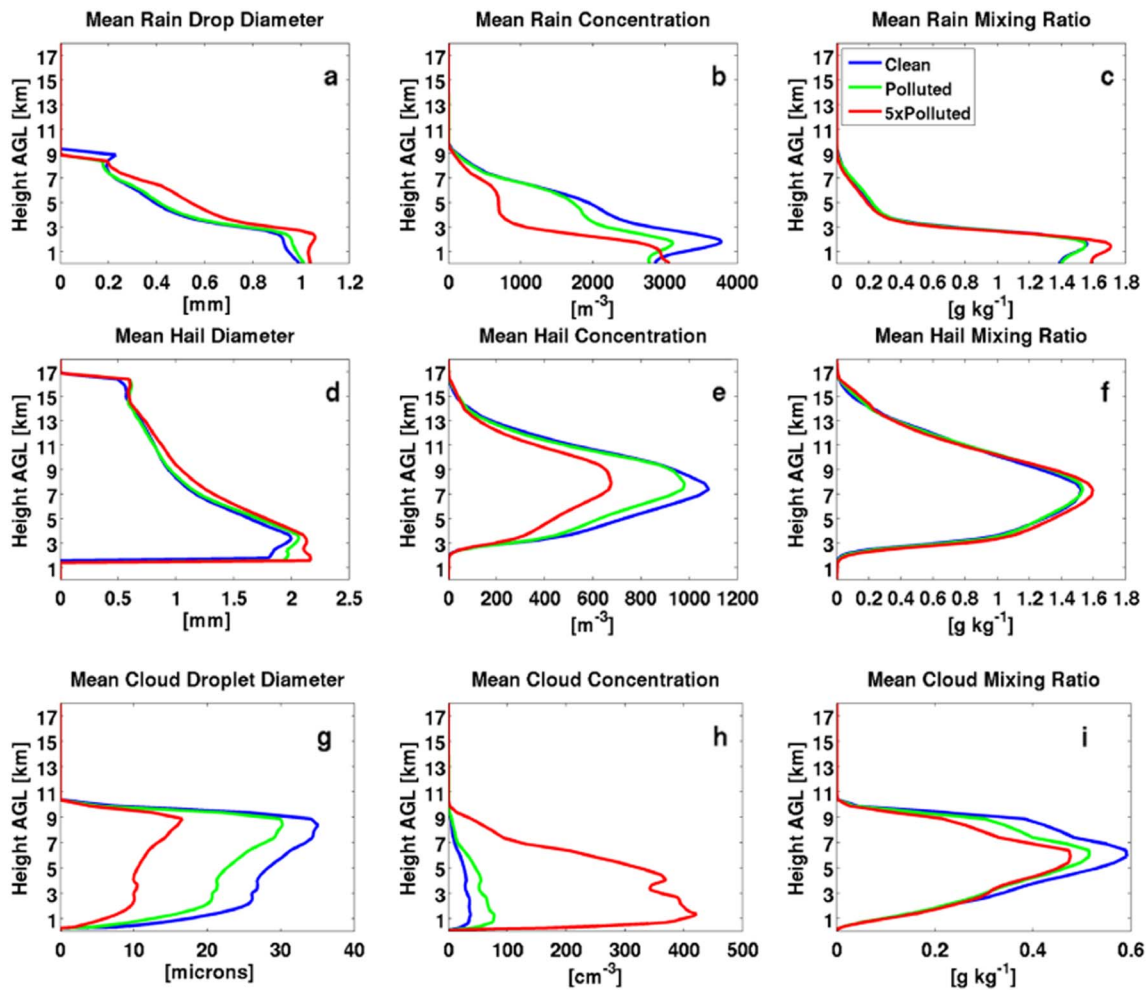


Fig. 18. Spatial and temporal means during 0630–1730 UTC in the convective region within the Clean (blue), Polluted (green) and $5 \times$ Polluted (red) of: (a) rain drop diameter [mm], (b) rain concentration [m^{-3}], (c) rain mixing ratio [g kg^{-1}], (d) hail diameter [mm], (e) hail concentration [m^{-3}], (f) hail mixing ratio [g kg^{-1}], (g) cloud droplet diameter [microns], (h) cloud droplet concentration [cm^{-3}] and (i) cloud droplet mixing ratio [g kg^{-1}]. (For interpretation of the references to color in this figure legend, the reader is referred to the web version of this article.)

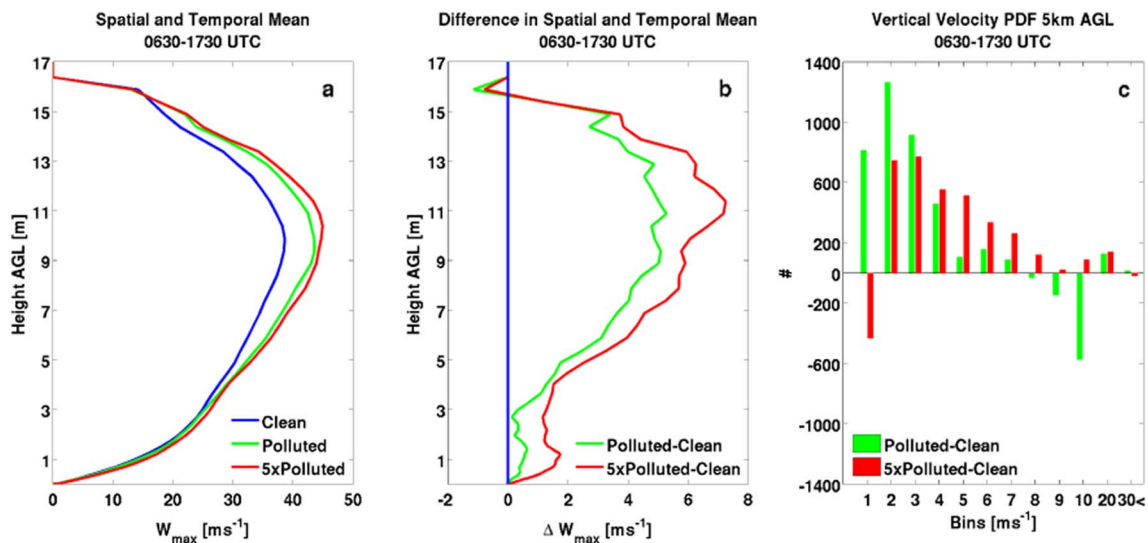


Fig. 19. (a) Spatial and temporal mean of the maximum updraft velocity within the convective region during 0630–1730 UTC for the Clean (blue), Polluted (green) and $5 \times$ Polluted (red). (b) Difference in the spatial and temporal means of the maximum updraft velocity of Polluted (green) and $5 \times$ Polluted (red) to Clean. (c) Relative Probability Density Function (PDF) of updrafts velocity at 5 km AGL during 0630–1730 UTC between the Polluted (green) and $5 \times$ Polluted (red) simulations and the Clean simulation. (For interpretation of the references to color in this figure legend, the reader is referred to the web version of this article.)

three of the simulations produced an MCS that was comparable to the storm observed in terms of the MCS location, genesis time, and total precipitation quantities. While the total amount of precipitation did not differ substantially among the simulations, changes in aerosol concentrations altered the precipitation characteristics within the three simulations in the following ways:

- Greater aerosol concentrations were shown to decrease the total area of the MCS precipitation while increasing the area with heavier accumulated precipitation.
- Greater aerosol concentrations led to a decrease in the formation of stratiform precipitation and an increase in convective precipitation within the MCS.
- In the convective region, several processes likely contributed to an increase of precipitation: (1) The very humid environment of this storm, that enhanced amount of cloud water available to be collected which overwhelmed the reduction in precipitation efficiency associated with the aerosol-induced production of smaller droplets leading to a net increase in the conversion of cloud droplets to precipitation. (2) Convective invigoration since updraft velocities are enhanced as aerosol pollution levels are enhanced.
- Changes in aerosol concentrations reduced the amount of stratiform precipitation produced by the MCS due to the impacts of higher aerosol concentrations on the hydrometeor distribution within the two flows contributing to the stratiform-anvil: convective outflow and mesoscale slantwise ascent in which the aerosols originated above the boundary layer.
- Higher aerosol concentrations within the free troposphere led to more numerous smaller cloud droplets within the region of slow mesoscale ascent, which decreased collision-coalescence as well as riming rates within the stratiform-anvil.
- These simulations have shown that MCS precipitation formation characteristics are sensitive to the number of aerosols serving as potential CCN, in both the convective and regions of mesoscale ascent.

In Part 2, the impacts of enhanced aerosol concentrations on storm dynamics, specifically, the intensity of the straight-line winds (derecho) are examined.

Acknowledgements

The authors wish to thank Dr. Lewis Grasso for producing the synthetic satellite imagery and help with the Lagrangian parcel model, as well as his suggestions and input in simulating the 8 May 2009 case study MCS. This work was funded by the National Science Foundation under grant AGS-1005041.

References

Albrecht, B.A., 1989. Aerosols, cloud microphysics, and fractional cloudiness. *Science* 245, 1227–1230.

Alexander, G.D., Cotton, W.R., 1998. The use of cloud-resolving simulations of mesoscale convective systems to build a mesoscale parameterization scheme. *J. Atmos. Sci.* 55 (12), 2137–2161.

Altartaz, O., Koren, I., Remer, L.A., Hirsch, E., 2014. Review: cloud invigoration by aerosols-coupling between microphysics and dynamics. *Atmos. Res.* 140, 38–60.

Andreae, M.O., Rosenfeld, D., Artaxo, P., Costa, A.A., Frank, G.P., Longo, K.M., Silva-Dias, M.A.F., 2004. Smoking rain clouds over the Amazon. *Science* 303, 1337–1342.

Augustine, J.A., Caracena, F., 1994. Lower-tropospheric precursors to nocturnal MCS development over the central United States. *Weather Forecast.* 9 (1), 116–135.

Berg, W., L'Ecuyer, T., van den Heever, S., 2008. Evidence for the impact of aerosols on the onset and microphysical properties of rainfall from a combination of satellite observations and cloud-resolving model simulations. *J. Geophys. Res.* 113, D14S23.

Bey, I., Jacob, D.J., Yantosca, R.M., Logan, J.a., Field, B.D., Fiore, A.M., Li, Q.-B., Liu, H.-Y., Mickley, L.J., Schultz, M.G., 2001. Global modeling of tropospheric chemistry with assimilated meteorology: model description and evaluation. *J. Geophys. Res.* 106, 73–95.

Bowen, E.G., 1951. Radar observations of rain and their relation to mechanisms of rain formation. *J. Atmos. Terr. Phys.* 1 (3), 125–140.

Carrio, G.G., Cotton, W.R., 2011. Investigations of aerosol impacts on hurricanes: virtual seeding flights. *Atmos. Chem. Phys.* 11, 2557–2567.

Churchill, D.D., Houze, R.A., 1984. Development and structure of winter monsoon cloud clusters on 10 December 1978. *J. Atmos. Sci.* 41, 933–960.

Coniglio, M.C., Corfidi, S.F., Kain, J.S., 2011. Environment and early evolution of the 8 May 2009 Derecho-producing convective system. *Mon. Weather Rev.* 139, 1083–1102.

Coniglio, M.C., Corfidi, S.F., Kain, J.S., 2012. Views on applying RKW theory: an illustration using the 8 May 2009 Derecho-producing convective system. *Mon. Weather Rev.* 140 (3), 1023–1043.

Cotton, W.R., George, R.L., Wetzel, P.J., McAnelly, R.L., 1983. A long-lived mesoscale convective complex. Part I: the mountain-generated component. *Mon. Weather Rev.* 111 (10), 1893–1918.

Cotton, W.R., Lin, M.S., McAnelly, R.L., Tremback, C.J., 1989. A composite model of mesoscale convective complexes. *Mon. Weather Rev.* 117 (4), 765–783.

Cotton, W.R., Weaver, J.F., Beiler, B.A., 1995. An unusual summertime downslope wind event. *Weather Forecast.* 10, 786–797.

Cotton, W.R., Pielke Sr., R.A., Walko, R.L., Liston, G.E., Tremback, C.J., Jiang, H., McAnelly, R.L., Harrington, J.Y., Nicholls, M.E., Carrio, G.G., McFadden, J.P., 2003. RAMS 2001: current status and future directions. *Meteorog. Atmos. Phys.* 82, 5–29.

Cotton, W.R., Bryan, G.H., van den Heever, S.C., 2010. Storm and Cloud Dynamics - The Dynamics of Clouds and Precipitating Mesoscale Systems, International Geophysics.

DeMott, P.J., Prenni, A.J., Liu, X., Kreidenweis, S.M., Petters, M.D., Twohy, C.H., Richardson, M.S., Eidhammer, T., Rogers, D.C., 2010. Predicting global atmospheric ice nuclei distributions and their impacts on climate. *Proc. Natl. Acad. Sci.* 107 (25), 11217–11222.

Evans, C., Weisman, M.L., Bosart, L.F., 2014. Development of an intense, warm-core mesoscale vortex associated with the 8 May 2009 “super derecho” convective event. *J. Atmos. Sci.* 71 (3), 1218–1240.

Fan, J., Yuan, T., Comstock, J.M., Ghan, S., Khain, A., Leung, L.R., Li, Z., Martins, V.J., Ovchinnikov, M., 2009. Dominant role by vertical wind shear in regulating aerosol effects on deep convective clouds. *J. Geophys. Res.* 114, 1–9.

Fan, J., Leung, L.R., Rosenfeld, D., Chen, Q., Li, Z., Zhang, J., Yan, H., 2013. Microphysical effects determine macrophysical response for aerosol impacts on deep convective clouds. *Proc. Natl. Acad. Sci. U. S. A.* 110, E4581–90.

Fujita, T.T., 1978. Manual of downburst identification for project NIMROD. Satellite and Mesometeorology Research Project. Department of the Geophysical Sciences, University of Chicago.

Grabowski, W., 2016. Oral Present. XVII Int. Conf. Clouds Precipitation, Manchester 25–29, July 2016.

Grasso, L.D., 1996. Numerical Simulation of the May 15 and April 26, 1991 Tornadoic Thunderstorm. Ph.D. dissertation. Colorado State University (151 pp. [Available from Department of Atmospheric Science, Colorado State University, Fort Collins, CO 80523]).

Grasso, L.D., Lindsey, D.T., 2011. An example of the use of synthetic 3.9 μm GOES-12 imagery for two-moment microphysical evaluation. *Int. J. Remote Sens.* 32, 2337–2350.

Grasso, L., Hillger, D.W., Schaaf, C.B., Wang, Z., Brummer, R., DeMaria, R., 2013. Use of MODIS 16-day albedos in generating GOES-R advanced baseline imager imagery. *J. Appl. Remote. Sens.* 7 (1), 073584.

Harrington, J.Y., 1997. The effects of radiative and microphysical processes on simulated warm and transition season Arctic stratus. Ph.D. dissertation. Colorado State University 289 pp. [Available from Department of Atmospheric Science, Colorado State University, Fort Collins, CO 80523].

Harrington, J.Y., Reisin, T., Cotton, W.R., Kreidenweis, S.M., 1999. Cloud resolving simulations of arctic stratus. Part II: Transitionseason clouds. *Atmos. Res.* 51, 45–75.

Haywood, J., Boucher, O., 2000. Estimates of the direct and indirect radiative forcing due to tropospheric aerosols: a review. *Rev. Geophys.* 38 (4), 513–543.

van den Heever, S.C., Cotton, W.R., 2004. The impact of hail size on simulated supercell storms. *J. Atmos. Sci.* 61 (13), 1596–1609.

van den Heever, S.C., Cotton, W.R., 2007. Urban aerosol impacts on downwind convective storms. *J. Appl. Meteorol. Climatol.* 46, 828–850.

van den Heever, S.C., Carrió, G.G., Cotton, W.R., DeMott, P.J., Prenni, A.J., 2006. Impacts of nucleating aerosol on Florida storms. Part I: mesoscale simulations. *J. Atmos. Sci.* 63, 1752–1775.

Hill, G.E., 1974. Factors controlling the size and spacing of cumulus clouds as revealed by numerical experiments. *J. Atmos. Sci.* 31, 646–673.

Houze, R.A., 2004. Mesoscale convective systems. *Rev. Geophys.* 42 (4).

Houze, R.a., Biggerstaff, M.I., Rutledge, S.a., Smull, B.F., 1989. Interpretation of Doppler weather radar displays of midlatitude mesoscale convective systems. *Bull. Am. Meteorol. Soc.* 70 (6), 608–619.

Igel, M.R., Drager, A.J., van den Heever, S.C., 2014. A CloudSat cloud object partitioning technique and assessment and integration of deep convective anvil sensitivities to sea surface temperature. *J. Geophys. Res. Atmos.* 119, 10515–10535.

Jankov, I., Grasso, L.D., Sengupta, M., Neiman, P.J., Zupanski, D., Zupanski, M., Lindsey, D., Hillger, D.W., Birkenheuer, D.L., Brummer, R., Yuan, H., 2011. An evaluation of five ARW-WRF microphysics schemes using synthetic GOES imagery for an atmospheric river event affecting the California coast. *J. Hydrometeorol.* 12, 618–633.

Jirak, I.L., Cotton, W.R., McAnelly, R.L., 2003. Satellite and radar survey of mesoscale convective system development. *Mon. Weather Rev.* 131 (10), 2428–2449.

Johns, R.H., Hirt, W.D., 1987. Derechos: widespread convectively induced windstorms. *Weather Forecast.* 2 (1), 32–49.

Kane, R.J., Chelius, C.R., Fritsch, J.M., 1987. Precipitation characteristics of mesoscale convective weather systems. *J. Clim. Appl. Meteorol.* 26 (10), 1345–1357.

Keene, K.M., Schumacher, R.S., 2013. The bow and arrow mesoscale convective structure. *Mon. Weather Rev.* 141, 1648–1672.

- Khain, A., Rosenfeld, D., Pokrovsky, A., 2005. Aerosol impact on the dynamics and microphysics of deep convective clouds. *Q. J. R. Meteorol. Soc.* 131, 2639–2663.
- Klemp, J.B., Wilhelmson, R.B., 1978. The simulation of three-dimensional convective storm dynamics. *J. Atmos. Sci.* 35, 1070–1096.
- Kogan, Y.L., Martin, W.J., 1994. Parameterization of bulk condensation in numerical cloud models. *J. Atmos. Sci.* 51, 1728–1739.
- Koren, I., Kaufman, Y.J., Remer, L.A., Martins, J.V., 2004. Measurement of the effect of Amazon smoke on inhibition of cloud formation. *Science* 303, 1342–1345.
- Koren, I., Kaufman, Y.J., Rosenfeld, D., Remer, L.A., Rudich, Y., 2005. Aerosol invigoration and restructuring of Atlantic convective clouds. *Geophys. Res. Lett.* 32, 1–4.
- Leary, C.A., Houze Jr., R.A., 1979. Melting and evaporation of hydrometeors in precipitation from the anvil clouds of deep tropical convection. *J. Atmos. Sci.* 36, 669–679.
- Lebo, Z.J., Morrison, H., 2014. Dynamical effects of aerosol perturbations on simulated idealized squall lines. *Mon. Weather Rev.* 142, 991–1009.
- Letcher, T., Cotton, W.R., 2014. The effect of pollution aerosol on wintertime orographic precipitation in the Colorado Rockies using a simplified emissions scheme to predict CCN concentrations. *J. Appl. Meteorol. Climatol.* 53, 859–872.
- Li, G., Wang, Y., Lee, K.H., Diao, Y., Zhang, R., 2009. Impacts of aerosols on the development and precipitation of a mesoscale squall line. *J. Geophys. Res. Atmos.* 114, 1–18.
- Lilly, D.K., 1962. On the numerical simulation of buoyant convection. *Tellus* 14, 148–172.
- Maddox, R.A., 1980. Mesoscale convective complexes. *Bull. Am. Meteorol. Soc.* 61 (11), 1374–1387.
- Maddox, R.A., 1983. Large-scale meteorological conditions associated with midlatitude mesoscale convective complexes. *Mon. Weather Rev.* 111 (7), 1475–1493.
- May, P.T., Bringi, V.N., Thurai, M., 2011. Do we observe aerosol impacts on DSDs in strongly forced tropical thunderstorms? *J. Atmos. Sci.* 68, 1902–1910.
- McAnelly, R.L., Cotton, W.R., 1986. Meso- β -scale characteristics of an episode of meso- α -scale convective complexes. *Mon. Weather Rev.* 114 (9), 1740–1770.
- Mesinger, F., Arakawa, A., 1976. Numerical methods used in atmospheric models. GARP Publication Series 14, WMO/ICSU Joint Organizing Committee 64 pp.
- Meyers, M.P., Walko, R.L., Harrington, J.Y., Cotton, W.R., 1997. New RAMS cloud microphysics parameterization. Part II: the two-moment scheme. *Atmos. Res.* 45, 3–39.
- Olsson, P.Q., Cotton, W.R., 1997a. Balanced and unbalanced circulations in a primitive equation simulation of a Midlatitude MCC. Part I: analysis of balance. *J. Atmos. Sci.* 54, 457–478.
- Olsson, P.Q., Cotton, W.R., 1997b. Balanced and unbalanced circulations in a primitive equation simulation of a midlatitude MCC. Part II: analysis of balance. *J. Atmos. Sci.* 54, 479–497.
- Parker, M.D., Johnson, R.H., 2000. Organizational modes of midlatitude mesoscale convective systems. *Mon. Weather Rev.* 128, 3413–3436.
- Petters, M.D., Kreidenweis, S.M., 2007. A physics single parameter representation of hygroscopic growth and cloud condensation nucleus activity. *Atmos. Chem. Phys.* 7, 1961–1971.
- Przybylinski, R.W., et al., 2010. The 08 May 2009 Missouri Derecho: Radar Analysis and Warning Implications over Parts of Southwest Missouri. In: 25th Conf. on Severe Local Storms, Denver, CO. Am. Meteorol. Soc. 3B.1.
- Rosenfeld, D., Lohmann, U., Raga, G.B., O'Dowd, C.D., Kulmala, M., Fuzzi, S., Reissell, A., Andreae, M.O., 2008. Flood or drought: how do aerosols affect precipitation? *Science* 321, 1309–1313.
- Rotunno, R., Klemp, J.B., Weisman, M.L., 1988. A theory for strong, long-lived squall lines. *J. Atmos. Sci.* 45 (3), 463–485.
- Saleeby, S.M., Cotton, W.R., 2004. A large-droplet mode and prognostic number concentration of cloud droplets in the Colorado State University regional atmospheric modeling system (RAMS). Part II: sensitivity to a Colorado winter snowfall event. *J. Appl. Meteorol.* 43, 182–195.
- Saleeby, S.M., Cotton, W.R., 2008. A binned approach to cloud-droplet riming implemented in a bulk microphysics model. *J. Appl. Meteorol. Climatol.* 47, 694–703.
- Saleeby, S.M., van den Heever, S.C., 2013. Developments in the CSU-RAMS aerosol model: emissions, nucleation, regeneration, deposition, and radiation. *J. Appl. Meteorol. Climatol.* 52, 2601–2622.
- Saleeby, S.M., Herbener, S.R., van den Heever, S.C., L'Ecuyer, T., 2015. Impacts of cloud droplet-nucleating aerosols on shallow tropical convection. *J. Atmos. Sci.* 72, 1369–1385.
- Seigel, R.B., van den Heever, S.C., Saleeby, S.M., 2013. Mineral dust indirect effects and cloud radiative feedbacks of a simulated idealized nocturnal squall line. *Atmos. Chem. Phys.* 13, 4467–4485.
- Seiki, T., Nakajima, T., 2014. Aerosol effects of the condensation process on a convective cloud simulation. *J. Atmos. Sci.* 71, 833–853.
- Sheffield, A.M., Saleeby, S.M., Van Den Heever, S.C., 2015. Aerosol-induced mechanisms for cumulus congestus growth. *J. Geophys. Res. Atmos.* 120, 8941–8952.
- Smagorinsky, J., 1963. General circulation experiments with the primitive equations. I. The basic experiment. *Mon. Weather Rev.* 91, 99–164.
- Squires, P., 1958. The microstructure and colloidal stability of warm clouds. *Tellus* 10, 262–271. <http://dx.doi.org/10.1111/j.2153-3490.1958.tb02012.x>.
- Stevens, R.G., Pierce, J.R., 2014. The contribution of plume-scale nucleation to global and regional aerosol and CCN concentrations: evaluation and sensitivity to emissions changes. *Atmos. Chem. Phys.* 14 (24), 13661–13679.
- Storer, R.L., van den Heever, S.C., 2013. Microphysical processes evident in aerosol forcing of tropical deep convective clouds. *J. Atmos. Sci.* 70, 430–446.
- Storer, R.L., van den Heever, S.C., Stephens, G.L., 2010. Modeling aerosol impacts on convective storms in different environments. *J. Atmos. Sci.* 67, 3904–3915.
- Sui, C.-H., Li, X., 2005. A tendency of cloud ratio associated with the development of tropical water and ice clouds. *Terr. Atmos. Ocean. Sci.* 16, 419–434.
- Tao, W.K., Simpson, J., Sui, C.H., Ferrier, B., Lang, S., Scala, J., Chou, M.D., Pickering, K., 1993. Heating, moisture, and water budgets of tropical and midlatitude squall lines: comparisons and sensitivity to longwave radiation. *J. Atmos. Sci.* 50 (5), 673–690.
- Tao, W.K., Li, X., Khain, A., Matsui, T., Lang, S., Simpson, J., 2007. Role of atmospheric aerosol concentration on deep convective precipitation: cloud-resolving model simulations. *J. Geophys. Res. Atmos.* 112(D24).
- Tao, W.K., Chen, J.P., Li, Z., Wang, C., Zhang, C., 2012. Impact of aerosols on convective clouds and precipitation. *Rev. Geophys.* 50 (2).
- Twomey, S., 1974. Pollution and the planetary albedo. *Atmos. Environ.* 8, 1251–1256.
- Twomey, S., 1977. The influence of pollution on the shortwave albedo of clouds. *J. Atmos. Sci.* 34 (7), 1149–1152.
- Velasco, I., Fritsch, J.M., 1987. Mesoscale convective complexes in the Americas. *J. Geophys. Res.* 92, 9591–9613.
- Walko, R.L., Band, L.E., Baron, J., Kittel, T.G., Lammers, R., Lee, T.J., Ojima, D., Pielke Sr., R.A., Taylor, C., Tague, C., Tremback, C.J., 2000. Coupled atmosphere–biophysics–hydrology models for environmental modeling. *J. Appl. Meteorol.* 39 (6), 931–944.
- Ward, D., Cotton, W., 2011. A method for forecasting cloud condensation nuclei using predictions of aerosol physical and chemical properties from WRF/Chem. *J. Appl. Meteorol. Climatol.* 50, 1601–1615.
- Ward, D.S., Eidhammer, T., Cotton, W.R., Kreidenweis, S.M., 2010. The role of the particle size distribution in assessing aerosol composition effects on simulated droplet activation. *Atmos. Chem. Phys.* 10, 5435–5447.
- Weisman, M.L., Evans, C., Bosart, L., 2013. The 8 May 2009 Superderecho: analysis of a real-time explicit convective forecast. *Weather Forecast* 28, 863–892.
- Xu, X., Xue, M., Wang, Y., 2015a. Mesovortices within the 8 May 2009 bow echo over the central United States: analyses of the characteristics and evolution based on doppler radar observations and a high-resolution model simulation. *Mon. Weather Rev.* 143, 2266–2290.
- Xu, X., Xue, M., Wang, Y., 2015b. The genesis of mesovortices within a real-data simulation of a bow echo system. *J. Atmos. Sci.* 72, 1963–1986.